Studies on proposed muon identification system for ALICE 3

A thesis Submitted
in Partial Fulfilment of the Requirements
for the Degree of

MASTER OF SCIENCE

by

Arpan Maity

to the

School of Physical Sciences

National Institute of Science Education and Research(NISER)

Bhubaneswar, India

May 15, 2024

To my teachers, beginning with the first and most influential, my mother.

DECLARATION

I hereby declare that I am the sole author of this thesis in partial fulfillment of the requirements for a postgraduate degree from National Institute of Science Education and Research (NISER). I authorize NISER to lend this thesis to other institutions or individuals for the purpose of scholarly research.

Signature of the Student
Date:

The thesis work reported in the thesis entitled **"Studies on proposed muon identification system for ALICE 3"** was carried out under my supervision, in the school of Physical Sciences at NISER, Bhubaneswar, India.

Signature of the thesis supervisor
School:
Date:

Signature of the thesis co-supervisor
School:
Date:

ACKNOWLEDGEMENTS

This project would remain incomplete without acknowledging the contributions of individuals who supported and guided me throughout its completion. Firstly, I extend my gratitude to my guide Prof. B. Mohanty for offering me the opportunity to work within the experimental high-energy physics group and for guiding me throughout the project. His insightful questions along with comments and suggestions, were invaluable to me. I am deeply grateful to Dr. V.K. S. Kashyap, my co-guide, for consistently providing unwavering support whenever it was needed. Additionally, I extend my thanks to Dr. R. Karnam, Dr. S.S. Dasgupta, Dr. R. Singh, and Dr. G. J. Tambave along with the members of the group for their invaluable insights and discussions on various aspects.

I would like to thank Mr. D. Barik and Mr. D. Kumar along with the members of CMRP, NISER for their technical assistance with hardware works relating to the hybrid RPC.

I am indebted to the senior PhD students who welcomed me into their group and made me feel included in all activities. I would also like to thank the members of the Muon ID collaboration of ALICE 3; without their help, this project would not have been possible.

Additionally, I am grateful to the faculties of NISER across all departments who have taught me various courses.

I express my gratitude to the Department of Atomic Energy (DAE) for the generous scholarship (DISHA) I received in the first year, and to the Department of Science and Technology (DST) for the KVPY scholarship I have been receiving since the second year.

Finally, heartfelt thanks to my family and friends for their unwavering support and encouragement throughout this journey.

ABSTRACT

ALICE 3, a proposed upgrade to the ALICE experiment at CERN will have a muon identification system with hadron absorber. The muon identification detector aims to detect muon with low transverse momentum (p_T $\sim$1.5 GeV/c) and study the exotic hadron states that decay via muon channel. There are three detector proposals for muon detection namely Scintillator-based detector, Multi Wire Proportional Counter (MWPC), and Resistive Plate Chamber (RPC). The material of choice for absober are magnetic (iron) or non-magnetic (stainless-steel).

This report outlines the study conducted on an RPC-based muon identification system using Geant4 and PYTHIA/Angantyr. The analysis evaluates the detector's performance based on muon detection efficiency and the efficiency of reconstructing J/ψ which decay with dimuon channel. The detection efficiency of muon with pseudorapidity range of $|\eta| < 1.25$ is found to be 69.02% and 68.37% at transverse momentum $p_T \sim 1.5$ GeV/c with non-magnetic absorber and magnetic absorber respectively for pp collisions. The muon detection efficiency for Pb-Pb collisions is similar to the pp collision case. The J/ψ reconstruction efficiency with the same acceptance for pp collisions is found to be higher than the ALICE 3 Letter of Intent (LOI) for $p_T < 4$ GeV/c for both types of absorber. Furthermore, a one-glass hybrid Resistive Plate Chamber (RPC) with one electrode glass and the other metal coated with a secondary electron multiplier has been developed with a novel design.

Contents

List of Figures

List of Tables

Chapter 1

Introduction

The fundamental forces of nature govern the interactions between particles. These forces include the strong, weak, electromagnetic, and gravitational interactions. In the framework of the Standard Model of particle physics, the fundamental particles are categorized into quarks, leptons and bosons. There are six different flavors of quarks (up(u), down(d), charm(c), strange(s), top(t), and bottom(b)), three types of leptons (electron(e), muon(μ), and tau(τ)), along with their corresponding neutrinos (electron neutrino(ν_e), muon neutrino(ν_μ), and tau neutrino(ν_τ)), four gauge bosons (photon(γ), W^+, W^-, and Z), and a Higgs boson. The electromagnetic force described by Quantum Electrodynamics (QED), is mediated by the photon. Its influence extends across long distances and governs the interactions between charged particles.

In contrast, the weak force operates at much shorter ranges. This force is carried by the W and Z bosons. The electroweak theory describes the weak interactions, which unifies electromagnetism with the weak force.

Complementing these interactions is the strong force described by the Quantum Chromodynamics (QCD). The strong force is mediated by gluons. QCD describes the formation of bound states of quarks known as hadrons. A hadron is called a meson if it has two quarks and a baryon if it has three quarks.

The multi-quark hadrons (tetra-quark and penta-quark) also called exotic hadrons were first predicted in 1964 by Murray Gell-Mann [1]. Since then there have been attempts to study exotic hadrons in different collider experiments. A Large Ion Collider Experiment (ALICE) at the LHC is a dedicated detector system to study heavy ion collisions. When heavy ions collide at relativistic speeds, they create an extremely high-energy density state with deconfined quarks and gluons known as Quark-Gluon Plasma (QGP). This state undergoes various phases with time eventually leading to the formation of hadrons. The hadrons, produced in these collisions, either

get detected directly or indirectly through their decay daughters in the detector. The high-energy particle collision processes are described by relativistic kinematics.

1.1 Relativistic Kinematics

According to the special theory of relativity, the shift in reference frame is governed by Lorentz transformations. The concerned frame is the lab frame and the frame of the colliding particles. The four position of a particle or an event is defined as (t, x, y, z) where t is the time coordinate and x, y, z are the space coordinates. Now, consider a frame L' which is moving with a velocity v as measured from a frame L along the x-axis. In that frame (L') we define the 4-$position$ as (t', x', y', z'). Consider the same particle or the event with 4-position (t, x, y, z) in the L frame provided for both these frames the origin coincides at $t = t' = 0$ [2].

Applying the Lorentz transformation,

$$t' = \gamma\left(t - \frac{vx}{c^2}\right) \tag{1.1}$$
$$x' = \gamma(x - vt) \tag{1.2}$$
$$y' = y \tag{1.3}$$
$$z' = z \tag{1.4}$$
$$\gamma = \frac{1}{\sqrt{1 - \frac{v^2}{c^2}}} \tag{1.5}$$

similarly if we write the variables for the L in terms of L',

$$t = \gamma\left(t' + \frac{vx'}{c^2}\right) \tag{1.6}$$
$$x = \gamma(x' + vt') \tag{1.7}$$
$$y = y' \tag{1.8}$$
$$z = z' \tag{1.9}$$

or,

$$ct' = \gamma(ct - \beta x) \tag{1.10}$$
$$x' = \gamma(x - \beta ct) \tag{1.11}$$

Where $\beta = \frac{v}{c}$,these equations can be written in the form of matrix as,

$$\begin{pmatrix} ct' \\ x' \\ y' \\ z' \end{pmatrix} = \begin{pmatrix} \gamma & -\beta\gamma & 0 & 0 \\ -\beta\gamma & \gamma & 0 & 0 \\ 0 & 0 & 1 & 0 \\ 0 & 0 & 0 & 1 \end{pmatrix} = \begin{pmatrix} ct \\ x \\ y \\ z \end{pmatrix} \tag{1.12}$$

The 4-vector(4-position) can also be represented as x^μ where $\mu \in (0, 1, 2, 3)$,where $x^0 = ct$, $x^1 = x$, $x^2 = y$, $x^3 = z$. x^μ is a contravariant vector which is related to the covariant vector with the relation $x^\mu = g^{\mu\nu}x_\nu$ .So,we can define a matrix for the transformation,

$$x^\mu = g^{\mu\nu}x_\nu \tag{1.13}$$

$$x^\mu = \begin{pmatrix} 1 & 0 & 0 & 0 \\ 0 & -1 & 0 & 0 \\ 0 & 0 & -1 & 0 \\ 0 & 0 & 0 & -1 \end{pmatrix} x_\nu \tag{1.14}$$

so,

$$x_\mu = g_{\mu\nu}x^\nu \tag{1.15}$$

I is the 4-dimensional length element defined as,

$$I = x^\mu x_\mu = (ct)^2 - (x^2 + y^2 + z^2) = (x^0)^2 - (x^1)^2 - (x^2)^2 - (x^3)^2 \tag{1.16}$$

I is a Lorentz invariant quantity. In collision with relativistic energy the convention is to consider the beam of the particle along the z-axis. In similar way to the position, momentum vector is also defined by a contravariant vector, where the components are $p^\mu = (p^0, p^1, p^2, p^3) = (E, p_x, p_y, p_z)$ where E is the energy of the particle , p_x, p_y, p_z are the momentum along their respective directions considering c = 1.

Collider Experiment

The 4-momentum for the two colliding particles can be written as $p_1 = (E_1, \mathbf{p_1})$ and $p_2 = (E_2, \mathbf{p_2})$, where p_1 and p_2 are the 4-momentum for the two particles with space components $\mathbf{p_1}$

and $\mathbf{p_2}$, and E_1 and E_2 are the energies of the two particles.

$$s = (p_1 + p_2)^2 = (E_1 + E_2)^2 - (\mathbf{p_1} + \mathbf{p_2})^2 \tag{1.17}$$

$$= E_{cm}^2 \tag{1.18}$$

$$s = E_{cm}^2 = m_1^2 + m_2^2 + 2(E_1 \cdot E_2 + |\mathbf{p_1}| \cdot |\mathbf{p_2}|) \tag{1.19}$$

In the above case, we have considered that the collision is head-on. So, the angle between $\mathbf{p_1}$ and $\mathbf{p_2}$ is 180^o. We know that $E^2 = p^2c^2 + m^2c^4$ so, in natural units we have $E^2 - p^2 = m^2$. E_{cm} is the centre of mass energy.

1.1.1 Rapidity

A variable used to describe the kinematic condition of a particle is the *rapidity (y)*. The rapidity of a particle is defined in terms of its p_0 and p_z where $p_0 = E$ is the first component of the 4-momentum or energy and p_z is the momentum along z-direction[2],

$$y = \frac{1}{2} \ln \left(\frac{p_0 + p_z}{p_0 - p_z} \right) \tag{1.20}$$

Rapidity can be either positive or negative. The rapidity variable is dependent on the frame of reference. The rapidity of a particle in one reference frame is related by an additive constant to an other frame of reference.

$$y' = y - y_\beta \tag{1.21}$$

where y' is the rapidity of the particle in the L' frame and the rapidity of the particle in L is y. Where y_β is defined as the the rapidity of the frame L' with respect to L.

$$y_\beta = \frac{1}{2} \ln \left(\frac{1 + \beta}{1 - \beta} \right) \tag{1.22}$$

where $\beta = \frac{v}{c}$,and v is the velocity of the frame as seen from the L frame.

Further,y can be written as,

$$e^{y} = \sqrt{\frac{E + p_z}{E - p_z}} \tag{1.23}$$

$$e^{-y} = \sqrt{\frac{E - p_z}{E + p_z}} \tag{1.24}$$

From the relations,

$$\sinh(y) = \frac{1}{2}(e^{y} - e^{-y}) \tag{1.25}$$

$$\cosh(y) = \frac{1}{2}(e^{y} + e^{-y}) \tag{1.26}$$

we get,

$$E = m_T \cosh(y) \tag{1.27}$$

$$p_z = m_T \sinh(y) \tag{1.28}$$

Where,

$$m_T = \sqrt{m^2 + p_T^2} \tag{1.29}$$

$$p_T = \sqrt{p_x^2 + p_y^2} = \sqrt{|\mathbf{p}|^2 - p_z^2} \tag{1.30}$$

m_T is defined as the **transverse mass** and p_T is defined as the **transverse momentum**.

1.1.2 Pseudorapidity

Pseudorapidity (η) is another variable which is used to define the kinematic condition of a particle in relativistic collision in terms of momentum and is defined as[2],

$$\eta = \frac{1}{2} \ln \left(\frac{|\mathbf{p}| + p_z}{|\mathbf{p}| - p_z} \right) \tag{1.31}$$

where $|\mathbf{p}|$ is the the value of the total space momentum $|\mathbf{p}| = \sqrt{p_x^2 + p_y^2 + p_z^2}$ and the p_z is the momentum along the z-axis. For high energy collision it is convenient to consider the η, η is also

defined as,

$$\eta = -\ln(\tan\frac{\theta}{2}) \tag{1.32}$$

In many experiments the detector can provide information about the angle of the particles with respect to the beam axis thus, pseudo-rapidity is an important variable for those experiments. The variable rapidity y can be expressed in the form of η as,

$$y = \frac{1}{2}\ln\left[\frac{\sqrt{p_T^2\cosh^2\eta + m^2} + p_T\sinh\eta}{\sqrt{p_T^2\cosh^2\eta + m^2} - p_T\sinh\eta}\right] \tag{1.33}$$

In a similar we can express the η is terms of y

$$\eta = \frac{1}{2}\ln\left[\frac{\sqrt{m_T^2\cosh^2 y - m^2} + m_T\sinh y}{\sqrt{m_T^2\cosh^2 y - m^2} - m_T\sinh y}\right] \tag{1.34}$$

The pseudorapidity η can be very useful for the study with detector where only the geometry information is taken into account in terms of position. The value of angle θ can be obtained as,

$$\theta = \tan^{-1}\left(\frac{\sqrt{x^2+y^2}}{z}\right) \tag{1.35}$$

where x, y are the positions in geometry in cartesian coordinates. The arctan function ranges from $-\frac{\pi}{2}$ to $\frac{\pi}{2}$ which requires $atan2$ for implementation which maps the positive y axis as 0 to π and the negative y axis as 0 to $-\pi$, where 0 common for both.

1.1.3 Azimuthal angle

Azimuthal angle is defined as the angel extended by the transverse momentum in the transverse plane and is given by,

$$\phi = \tan^{-1}\frac{p_y}{p_x} \tag{1.36}$$

In the detector geometry the azimuthal angle is given by,

$$\phi = \tan^{-1}\frac{y}{x} \tag{1.37}$$

where x and y are positions in detector geometry in cartesian coordinates. To implement this similar approach of $atan2$ must be considered.

1.2 Study of exotic hadrons in ALICE 3

In the year 2003, Belle collaboration discovered the first heavy exotic hadron called χ_{c1}[3]. This exotic hadron has been observed in various experiments including at the LHC by CMS, ATLAS, and LHCb in the recent past. Even with all these efforts we still do not have a conclusive idea about the nature of this exotic hadron. It has been proposed that this can be a "diquark-diantiquark" pair or $D^0\bar{D}^{*0}$ "molecule". Therefore it is both interesting and challenging to study the existence and the nature of exotic hadrons. Moreover, high precision measurement of transverse momentum (p_T) with rapidity (y) dependence of exotic states (Quarkonium) will allow us to describe the dynamics of these states within the QGP medium more accurately.

Relativistic heavy ion collisions can be a tool to study the properties of exotic hadrons within a medium of deconfined color charges. studying such collisions will allow us to put constraints on the properties of exotic states including binding potential and hadronization mechanisms [4]. Certain statistical models [5] has predicted that the production of exotic hadrons in the low p_T region ($p_T < 5 - 6$ GeV/c) might be enhanced with medium induced or medium enhanced mechanisms.

The detector system of ALICE is set to have an upgrade, called ALICE 3. ALICE 3 aims to study quarkonia down to zero p_T, for these studies, the detector capabilities are planned to be increased to detect muon(μ) at mid-rapidity ($y \approx 0$) and study the quarkonia which decay with muon channel. Thus, a muon identification detector has been planned to identify muon down to low $p_T \sim 1.5$ GeV/c at $\eta = 0$, where η is the pseudorapidity.

This provides a unique p_T reach to study the formation and dissociation of χ_{c1} in heavy ion collisions at thermal momentum scales. The other such facility in CMS has a p_T reach greater than 10 GeV/c. Moreover, no LHC experiment will have the capability to measure J/ψ decays below 6 - 7 GeV/c with high purity. The limitations of CMS and ATLAS detector systems result in the non-zero acceptance for the $\chi_{c1} \rightarrow J/\psi\gamma \rightarrow \mu^+\mu^-\gamma$ decay channel in pp collisions only for $p_T > 10$ GeV/c. Moreover, the other decay channel measurement $\chi_{c1}(3872) \rightarrow (J/\psi)\pi^+\pi^-$ are also with the limitation of $p_T > 10$ GeV/c [4].

The proposed muon identification system will cover a pseudo-rapidity $|\eta| < 1.25$. There are three proposed detected systems for the muon identification detector which include scintillator-based, Multi Wire Proportional Counter (MWPC), and Resistive Plate Chamber (RPC). More-

over, there is a proposal to have a hadron absorber of magnetic or non-magnetic material, where the magnetic material is iron and the non-magnetic material is stainless steel [4]. This study aims to find the performance of the muon identification detector with the muon detection efficiency and J/ψ reconstruction efficiency which decay with the dimuon channel. It also amis to find the effect of the choice of absorber material on the detector performance.

1.3 Hybrid RPC

RPCs are gas-based detectors with a very good position and time resolution, but they are operated with gases which have very high global warming potential (freon) and contribute to global warming. There have been attempts to utilize other gas mixtures and reduce the gas flow rate of standard RPC gas without compromising the detector characteristics in terms of efficiency and resolution in position and time. One such attempt has been made to reduce the gas flow rate with a hybrid model of one glass RPC where one electrode is a glass and the other is a metal coated with a secondary electron multiplier. The secondary electron multiplier is a metal oxide which is coated on the anode metal electrode and the cathode is the glass electrode coated with a conductive paint. It has been found that this model has efficiency comparable to standard two-glass RPCs even with low standard RPC gas flow rate[6].

Chapter 2

Muon Identification in ALICE 3

2.1 Detectors in ALICE 3

The planned enhancement of the ALICE detector configuration is intended to operate during the run-5 and run-6 periods of the LHC. In the proposed ALICE 3 detector systems from the beam pipe to the outer surface, the first detector system is the vertex detector which is followed by the trackers. The trackers are followed by the TOF (Time of flight detectors) which is placed inside the RICH (Ring Imaging Cherenkov Detectors). At the outer surface of RICH, there will be ECal (Electromagnetic calorimeters) followed by the superconducting magnet systems. These detectors will be followed by an absorber of Iron (magnetic) or Stainless steel (non-magnetic). The muon identification detectors called muon chamber will be starting approximately at a radius of 3 m. The absorber below the muon chamber will be of approximately 10^3 t (1 kilo ton) in the form of a conical tube (The outer and the inner radius decreases from the center of the detector geometry to both ends along the beam axis.), an FCT (Forward conversion Tracker) will also be placed in a dedicated dipole magnet. The schematic of the proposed ALICE 3 detector setup [4] is shown in Figure 2.1 and their corresponding proposed layout [4] in the Figure 2.2

2.2 Muon identification detector for ALICE 3

Muon, classified as a lepton, possesses a mass of 105.658 MeV and a lifetime of 2.197 seconds [7]. It carries the same charge as an electron. Muons are intriguing particles due to their remarkable ability to penetrate materials deeply. Three types of detector systems have been proposed for the ALICE 3 muon identification, they are scintillator, Multi Wire Proportional Counter (MWPC),

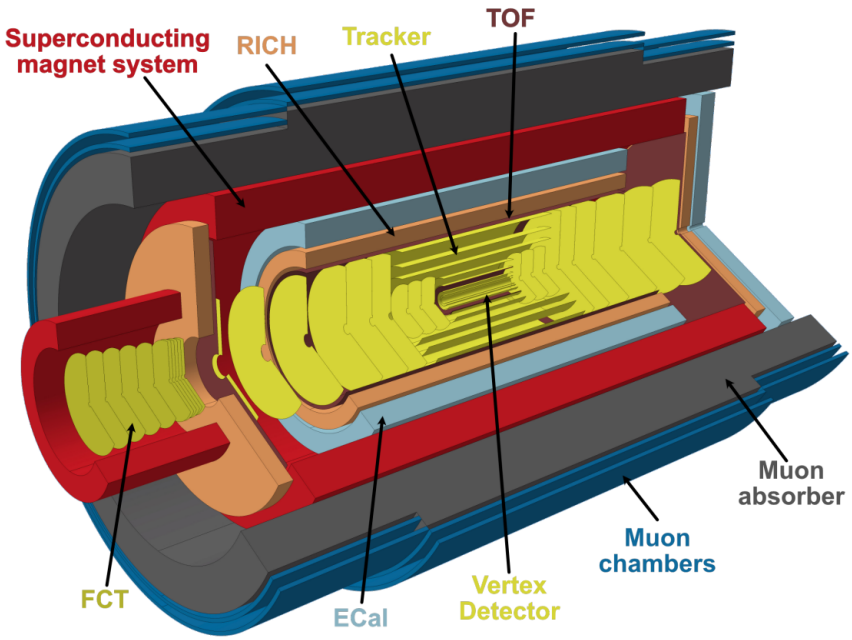

Figure 2.1: Schematic of the ALICE 3 detector setup

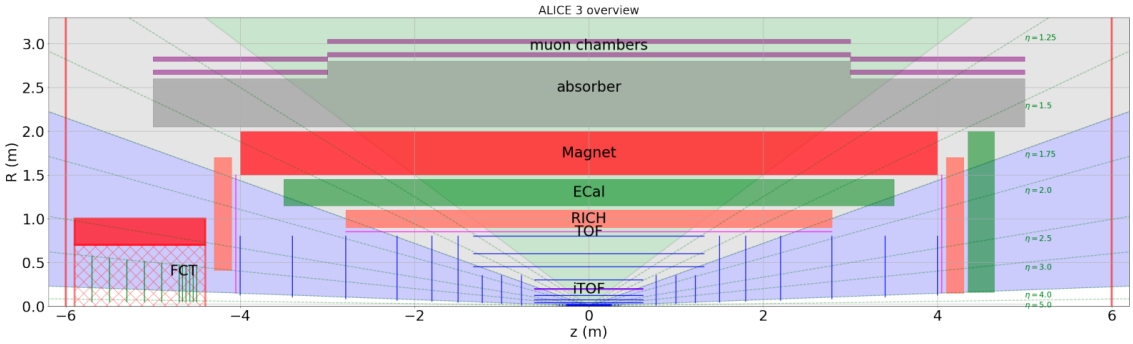

Figure 2.2: Proposed ALICE 3 detector setup

and Resistive Plate Chamber (RPC). Muon identification in ALICE 3 relies on aligning data from the tracker and the muon identification chamber. The muon identification process involves reconstructing tracklets in the muon identifier, which are straight segments connecting pairs of space points in two layers of chambers. To match information from the internal tracker and the muon identifier, each track is extrapolated to the muon identification chamber, considering magnetic field effects and energy loss.

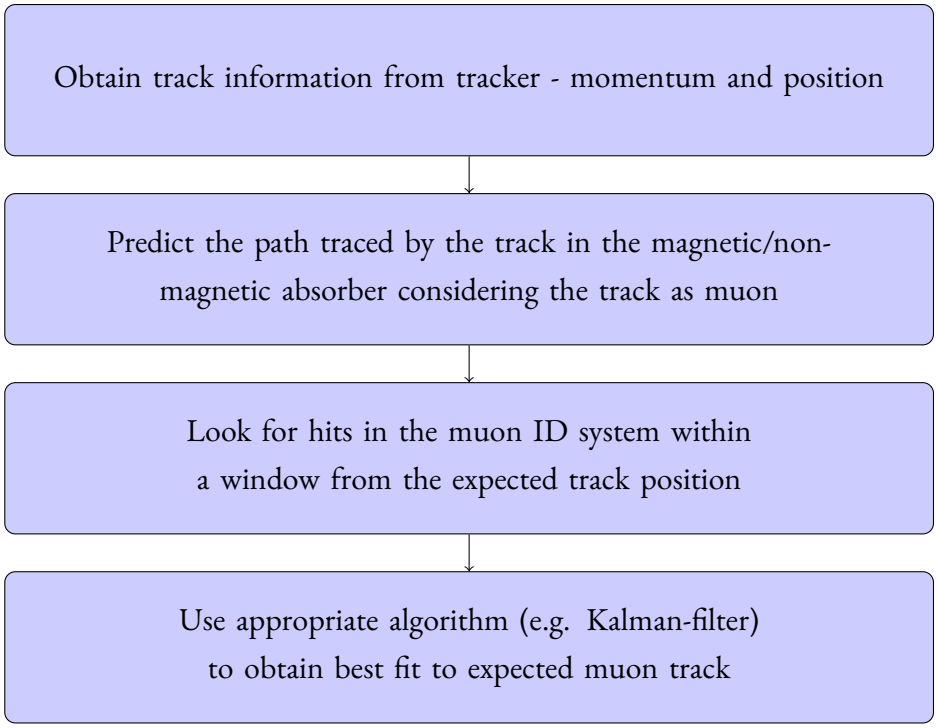

2.3 The RPC based system

Out of the three proposed detectors, we have studied the RPC. RPCs are gaseous detectors and are very efficient muon detectors. They are inexpensive, can cover large area and provide reasonable position ($\sim$1 cm) and excellent time resolution ($\sim$1 ns) [8]. The proposal is to have two layers of RPCs at a radii of 3.01 m and 3.16 m with respect to the beam axis forming the muon identification (ID) chamber of ALICE 3. More details on the working and construction of RPC are given in Appendix A.

2.3.1 The RPC geometry and absorber

The RPC has 5 components and their dimensions are tabulated in Table 2.1. In this study the electrode of the RPC is chosen to be glass coated with the conducting paint (e.g. graphite), there are other choices as well (e.g. bakelite). The width of the strips is 4.9 cm and same for the both the layers of the muon ID chamber. The pitch is taken to be 5cm resulting in a gap of 1 mm in between the strips.

The image in the Figure 2.3 has been obtained with `solidworks` [9]. The width of the frame in the RPC assembly is 1 cm making the active area of the detector 1.10×1.10 m^2 and 1.15×1.15 m^2 for RPC at radii of 3.01 m and 3.16 m respectively. The two layers of strips are

Material (component)	Dimension(in m) Layer 1 (at 3.01 m)	Dimension (in m) Layer 2 (at 3.16 m)
FR4 (epoxy) (in blue, Fig. 2.3)	$1.120 \times 1.120 \times 0.001$	$1.170 \times 1.170 \times 0.001$
Strips (Copper) (in yellow, Fig. 2.3)	$1.100 \times 0.049 \times (40 \times 10^{-6})$	$1.150 \times 0.049 \times (40 \times 10^{-6})$
Mylar (in red, Fig. 2.3)	$1.120 \times 1.120 \times (250 \times 10^{-6})$	$1.170 \times 1.170 \times (250 \times 10^{-6})$
Glass (in sky blue, Fig. 2.3)	$1.120 \times 1.120 \times 0.002$	$1.170 \times 1.170 \times 0.002$
Frame (polycarbonate) (in magenta, Fig. 2.3)	$1.120 \times 1.120 \times 0.002$	$1.170 \times 1.170 \times 0.002$

Table 2.1: The Proposed RPC geometry.

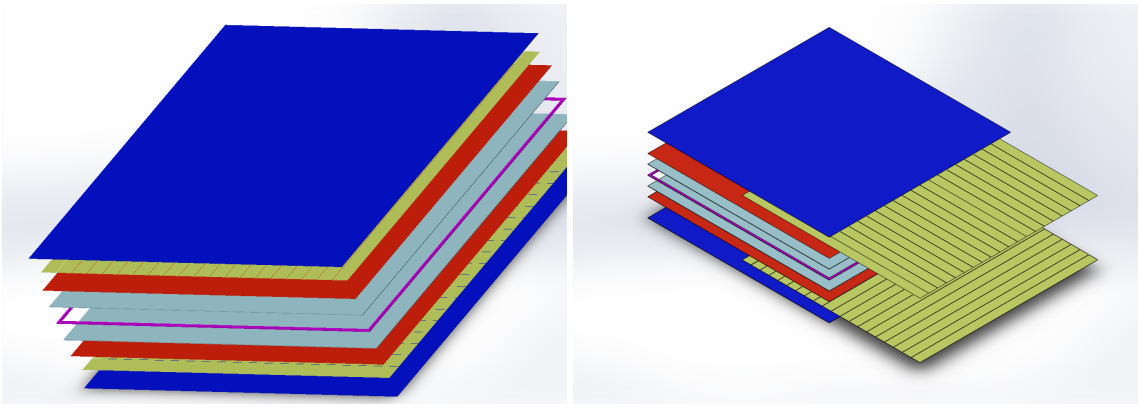

(a) (b)

Figure 2.3: (a)An assembly of the RPC, (b) expanded view of the strips in RPC.

perpendicular to each other in the RPC as shown in the Figure 2.3b, where the strips has been shown as expanded view. The RPCs at radii of 3.01 have 22 strips and at 3.16 m have 23 strips.

The absorber geometry is shown in Figure 2.4. The figure has been obtained with `solidworks` [9]. The dimensions of the absorber are tabulated in Table 2.2. Note that the geometry of the absorber is of the form of a conical tube with maximum thickness at the centre ($\eta \approx 0$) and it reduces towards both the ends along the beam axis ($|\eta| > 0$). This is because the path length of a particle with $\eta \approx 0$ will traverse less distance in space than a particle with $|\eta| > 0$ to reach the same radius in the x, y plane (plane perpendicular to the beam axis). The studies on the determination of absorber dimension is ongoing, the dimension of the absorber geometry at this stage are preliminary.

17 assemblies (Figure 2.3 is one assembly) make one **sector(ring)** and **9 sectors of 2 layers** make

the complete muon ID chamber. Therefore the total number of RPCs required to cover the complete geometry of the muon ID chamber is $17 \times 9 \times 2 = 306$ with 153 RPCs in each layer.

Part	Inner radius (m)	Outer radius (m)	length (m)	centre position of tube (x, y, z)(m)
Part 1 (see Fig. 2.4)	2.200	2.900	2	(0.0, 0.0, 0.0)
Part 2(i) (see Fig. 2.4)	2.225	2.875	1	(0.0, 0.0, 1.5)
Part 2(ii)(see Fig. 2.4)	2.225	2.875	1	(0.0, 0.0,-1.5)
Part 3(i) (see Fig. 2.4)	2.275	2.825	1	(0.0, 0.0, 2.5)
Part 3(ii)(see Fig. 2.4)	2.275	2.825	1	(0.0, 0.0,-2.5)
Part 4(i) (see Fig. 2.4)	2.325	2.775	1	(0.0, 0.0, 3.5)
Part 4(ii)(see Fig. 2.4)	2.325	2.775	1	(0.0, 0.0,-3.5)
Part 5(i) (see Fig. 2.4)	2.360	2.740	1	(0.0, 0.0, 4.5)
Part 5(ii)(see Fig. 2.4)	2.360	2.740	1	(0.0, 0.0,-4.5)

Table 2.2: The absorber Geometry in ALICE 3.

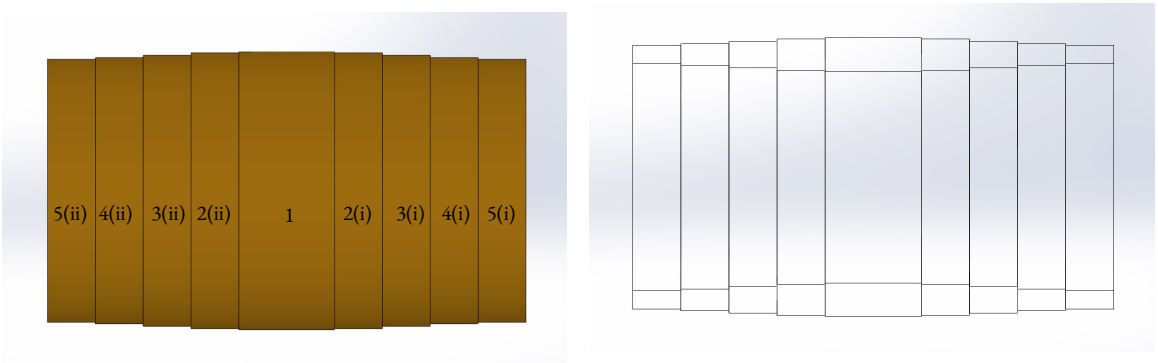

(a) (b)

Figure 2.4: (a) Schematic of the absorber geometry, (b) Schematic of the absorber in transperant view.

There are two choices for the **absorber material, magnetic and non-magnetic**. The **magnetic** absorber material is **iron** and the **non-magnetic** absorber is **stainless steel** [4]. The material budget of the magnetic absorber is much less than the non-magnetic absrober. The magnetic absrober choice will require the extrapolation of the muon path from a radius less the inner radius of the absorber till the muon ID chamber where as the muon track can be extrapolated linearly for the non-magnetic absorber case.

Chapter 3

Simulation of proposed ALICE 3 muon ID chamber

3.1 Implementation of muon ID chamber

In this study, we have simulated the RPC detector geometry in Geant4 and particle collisions with PYTHIA. PYTHIA is a monte carlo event generator. Initially, PYTHIA was a framework or model to study the p-p collision. The hadronization in PYTHIA is modelled with String fragmentation mechanism [10]. Later on, the Angantyr framework was introduced to study heavy ion collision. Geant4 is another toolkit developed by CERN, where one can define the geometry of different detectors and study their response. This can also be used to study the passage of particles through different materials [11, 12, 13] (Please refer to the Appendix B).

The collisions of particles are simulated in PYTHIA and information about produced particles during the collisions are feed into the Geant4 and thereafter Geant4 produces tracks of those particles considering the magnetic field in its path and the detector geometries. The implemented geometries are shown in Figure 3.1.

There is a sensitive layer at the radius of 2.19 m which is just for the purpose of the simulation in the study. Two million proton-proton(pp) collisions events were simulated and fifty thousand lead-lead ions(Pb-Pb) collisions events were simulated in PYTHIA and subsequently feed into the Geant4 to find the hit position for the particle tracks on the sensitive parts of the detector. The sensitive part of the RPC in this study is the gas volume in between in the glass.

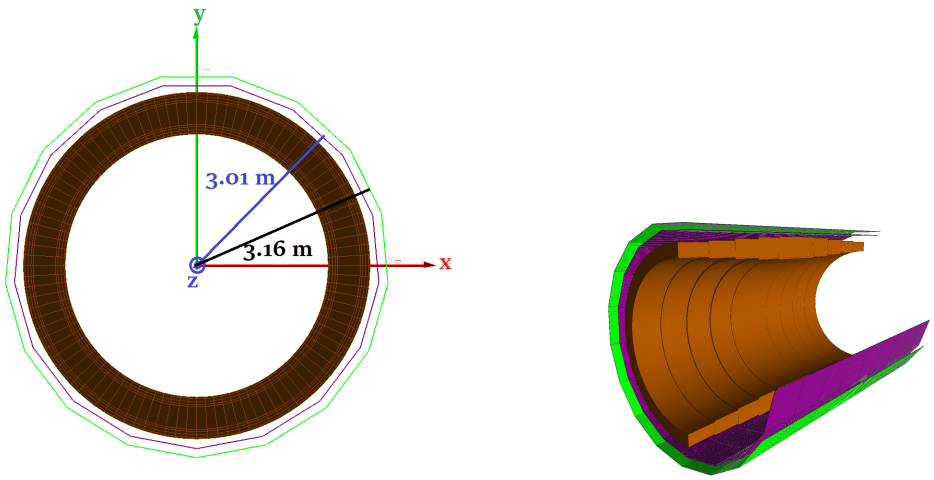

(a) (b)

Figure 3.1: (a) Transverse view of the muon ID , (b) longitudinal view of the muon ID as implemented in the Geant4.

3.1.1 PYTHIA configuration for pp collisions

1. Collision system : proton-proton(pp)
2. Energy of collisions: 14 TeV
3. No of events generated: 2×10^6
4. Event Generator Version- PYTHIA 8.309 + Geant 4.11.1
5. Interested particle: muon(μ), pion(π), kaon(K)

The PYTHIA configuration:

```
# beams
Beams :idA 2212 # proton
Beams :idB 2212 # proton
Beams :eCM 14000. # GeV
# processes
PhaseSpace : pTHatMin 0.5
PhaseSpace : pTHatMinDiverge = 0.5
Charmonium :: all = on
# decays
HadronLevel : Decay on
443: mayDecay = on
```

3.1.2 PYTHIA configuration for Pb-Pb collisions

1. Collision system : lead-lead(Pb-Pb)
2. Energy of collisions: 5.52 TeV
3. No of events generated: 5×10^4
4. Event Generator Version- PYTHIA 8.309 + Geant 4.11.1
5. Interested particle: muon(μ), pion(π), kaon(K)

The PYTHIA/Angantyr configuration:

```
# beams
Beams:idA 1000822080  # Pb
Beams:idB 1000822080  # Pb
Beams:eCM 5520.0    # GeV
# processes
HardQCD:all on
MultipartonInteractions:bProfile = 3
MultipartonInteractions:processLevel=3
HeavyIon:SigFitNGen 20
HeavyIon:SigFitDefPar 14.82,1.82,0.25,0.0,0.0,0.0,0.0,0.0
HeavyIon:bWidth 10.0
PhaseSpace:pTHatMin 0.5
PhaseSpace:pTHatMinDiverge = 0.5
Charmonium::all = on
# decays
HadronLevel:Decay on
443:onMode = off
443:onIfAny = 13 -13
13:onMode=off
-13:onMode=off
```

The output of the Geant4 is stored as ROOT file format and analysed with the CERN ROOT software[14]. To reduce the file storage only the information of the hit particles are stored along with the particle produced at the generator level, PYTHIA before feeding it to Geant4 (**for implementation check** [15]).

3.2 Digitization of strips

RPC is gas based detector which works with the principle of electron multiplication in gas. The electron multiplication in the gas results in avalanche formation of charges. Therefore, when the avalanche size is large, there is a chance that the signal can be induced on more than one strip. There can be situations when the avalanche formation happens with charge particle passing through the gap (space) in between two strips, in such a case the avalanche formation might induce signal on the strips adjacent to the gap. The schematic of an avalanche in shown in Figure 3.2, the electric field between the two glass electrodes is E_0. The electric field within the avalanche region is E_2, because the movement of the charges is influenced by the electrodes and resulting electric field from that movement within the avalanche region is opposite to the field of the electrodes, the effective electric field E_2 is less than E_0. On the other hand, the effective electric field E_1 and E_3, between the ends of the avalanche region and the electrodes gets enhanced and are greater than E_0. Furthermore, when signal is induced on a strip due to a muon track, the po-

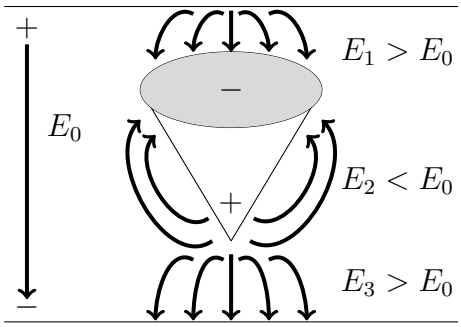

Figure 3.2: Schematic of avalanche.

sition information of the muon track obtained from the RPC is dependent on the size of the strip width. Instead of getting the exact position in terms of continuous value, the position is restricted to the discrete value dependent on the centre position of the strips along its width.

These phenomenons must be taken into account in simulation, the consideration of these phenomenons is **digitization** in this study. The digitization starts with the assumption that the avalanche formation of charges in the gas is of the form of a cone. Signal is induced on the strips which are situated within the area of the base of the cone. The radius of the cone base or in other words, avalanche size must be studied with simulation considering the gas composition used in the RPC, electric field and other parameters along with experimental studies with characterization of the prototype RPC. However in this study, the size of the avalanche or the radius of the

cone base is simulated randomly, which is a simple model of digitization.

3.2.1 Implementation of digitization

To implement the idea mentioned earlier the gas volume has been considered as sensitive. The Geant4 gives the position and momentum of the muon track passing through the gas volume. A circle is imagined with the centre at the hit position of the muon track in the gas volume and the radius chosen randomly from a probability density function. The strips which are within the area of that circle are considered to be fired. There are few assumptions for this implementation, which are following,

1. When signal is induced on more than one strips, their responses are simultaneous.
2. For a single muon hit, a maximum of 4 strips can be fired.
3. The probability density function for the radius of the base cone of avalanche, which is to be generated randomly is given by,

$$f(x) = \frac{1}{ax^2 + b} \tag{3.1}$$

$$a = 7 \tag{3.2}$$

$$b = 0.7 \tag{3.3}$$

The first assumption can be modified with introduction of time information, because RPCs have very good time resolution and the particle rate is highly reduced after the absorber this assumption is fine with our study. The second assumtion is based on the case when a muon is close or is exactly at the gap in between the strips, the corresponding strips adjacent to the gap will be induced making the number 2 but the induced charge in those strips can also induce their adjacent strips on both side resulting in the total number of induced strips to be 4. The probability density function must be a decaying function, which will ensure that the maximum number of time signal will be induced only on one strip. The choice of a and b has been taken such that the probability of the numbers less than 1 is maximum (or most of the time a single strip is induced), this was just a choice one can take other values or other function as well according to the findings of the simulation and experimental study. The obtained random number is less than 4 and greater than 0 and to estimate the radius we have the following condition,

$$r = \frac{4.9}{2} \times x \tag{3.4}$$

r is the radius of the circle to be imagined in the gas gap parallel to the glass planes and x is the random number obtained with the probability density function. To obtain the random number with the chosen probability distribution function we have followed the inversion technique. The cumulative density function has to be calculated for the probability distribution function.

$$F(x) = \int_0^x \frac{1}{at^2 + b} dt = \frac{\tan^{-1}\left(\frac{\sqrt{a}x}{\sqrt{b}}\right)}{\sqrt{ab}} \tag{3.5}$$

The inverse of the cumulative density function we have,

$$x = F^{-1}(u) \tag{3.6}$$

$$u = F(x) = \frac{\tan^{-1}\left(\frac{\sqrt{a}x}{\sqrt{b}}\right)}{\sqrt{ab}} \tag{3.7}$$

$$\frac{x}{\sqrt{\frac{b}{a}}} = \tan\left(\sqrt{ab}u\right) \tag{3.8}$$

$$x = \sqrt{\frac{b}{a}} \tan\left(\sqrt{ab}u\right) \tag{3.9}$$

The value of u is uniformly generated random number between 0 and 1 and the inverse cumulative density function gives the required values of x and the probability density of x. The random numbers were generated with the ROOT based pseudo random number generator `TRandom3`.

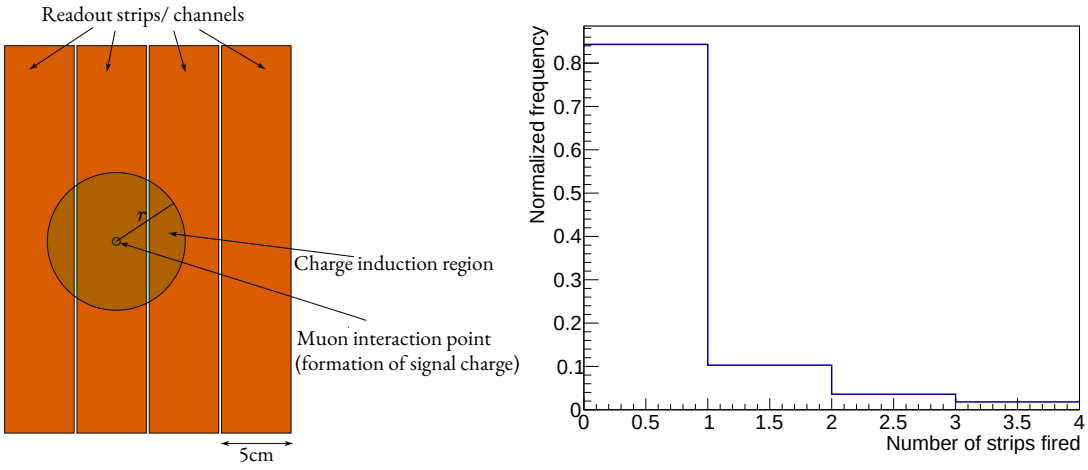

(a) (b)

Figure 3.3: (a) The schematic of digitization. (b) The normalised frequency of the number strips on which charge is induced.

The schematic of the digitization is shown in Figure 3.3a. It shows a situation when the number of strips fired or on which charge is induced is three in total. The strips are of dimension 4.9 cm and the gap between the strips is 0.1 cm making the pitch to be 5 cm. In the Figure 3.3b, the normalised frequency of the number of strips fired for the digitization scheme has been shown. It is evident that maximum number of times only single strip has been induced with very rare cases of four strips being induced. The simulation of the circle has to be with respect to the three dimensional geometry of the ALICE 3 muon ID chamber. There are two layers of RPCs in the muon ID chamber and for each RPC layer we have two strip layers. After digitization one strip layer will provide the information of the $x - y$ coordinate and the other strip layer will provide the information of the z coordinate for each RPC layer. The information for the z coordinate is easy to obtain. The pseudo-code and the algorithm is shown in Algorithm 1.

There can be four situations for the digitization scheme. The first, when the avalanche size is small and it is within the width of the strip. Second case when a complete strip is within the circle. Third, the left edge position of a strip is less than $\mathbf{z}+r$ but the right edge position is greater than $\mathbf{z}+r$ (edge of the circle is within the strip width). Fourth, the left edge of the strip is less than $\mathbf{z}-r$ but the right edge position is greater than $\mathbf{z}-r$ (also edge of the circle is within the strip width). The first situation can be implemented with the condition of the last two in which the the same strip will appear twice, but as the mean is considered the centre position of the same strip will appear with the digitized position of z-axis.
In the implementation the top layer of strips have the width along the z-axis and the bottom layer of strips have the width on the (x, y)-plane. The digitization of the strips to find the position for the $x - y$ axis requires little more modification to the algorithm. One method to find the digitized position of the strips can be to find the equation of the straight line for the each inclined orientation of the RPCs in a sector and then find the edges of induced circle in the $x - y$ axis which lie on those lines with the respect to the hit position of the muon in the gas volume (the centre of the circle). In the Figure 3.4, the scheme of the digitization for the $x - y$ axis is shown, the transverse section of the muon ID is shown in the left and the expanded view is shown in the right. The red coloured line is according to the orientation of a particular RPC of the sector as shown in the Figure 3.4. The extent of the circle (with randomly generated radius r) along that red line can be found from the equation of that line and the **(x,y)** coordinate of the muon interaction position (hit position in the gas volume). Finally the detector ID (each detector has a specific number) and the strip edge positions can be used to find the centre of the charge induced strips and their average gives the digitized $x - y$ position.

The other approach is bit different from this straight forward one and that has been imple-

Algorithm 1 Digitization scheme for z-axis

Input: Centre position (z-coordinate) of all the strips with width along z-axis, left and right edge (z-coordinate) of all the strips, random radius r, detector ID (0 to 153), z-coordinate of the hit position (**z**) in the gas volume
Output: Digitized z-coordinate value.
Create three arrays: `z_plus`, `z_minus`, `z_centre`
for each strip in the top strip layer of the RPCs **do**
    Store the z coordinate of edge towards +z axis in `z_plus`
    Edge towards -z axis in `z_minus`
    `z_centre` for centre of the strip, the indices of three should match.
end for
for Hit in the gas volume **do**
    Check the corresponding detector ID
    Find the indices of the above three arrays which are for that detector ID
    Create an array `z_temp`
    for Matched indices with the detector ID **do**
        If `z_minus[index]` $>$ **z** $- r$ and `z_plus[index]` $<$ **z** $+ r$:
            Store the `z_centre[index]` in `z_temp`
        End If
        If `z_minus[index]` $<$ **z** $- r$ and `z_plus[index]` $>$ **z** $- r$:
            Store the `z_centre[index]` in `z_temp`
        End If
        If `z_minus[index]` $<$ **z** $+ r$ and `z_plus[index]` $>$ **z** $+ r$:
            Store the `z_centre[index]` in `z_temp`
        End If
    end for
    `digit_z`= Mean of the elements in `z_temp`
    Return `digit_z`
end for

mented in this study. The symmetry of the arrangement of the RPCs in a sector (ring) has been utilised. The attempt is to reduce the dimension in the calculation. The vector forming with the center (beam axis) of the transverse plane ($x = 0, y = 0$) and the hit position in the gas volume is rotated with an angle such that the the resulting vector points towards to the RPC which lie on the x axis or perpendicular to the y axis (reference RPC). The angular difference or pitch between each of the RPCs in a sector (ring) is given by,

$$\phi = \frac{360^\circ}{17} \tag{3.10}$$

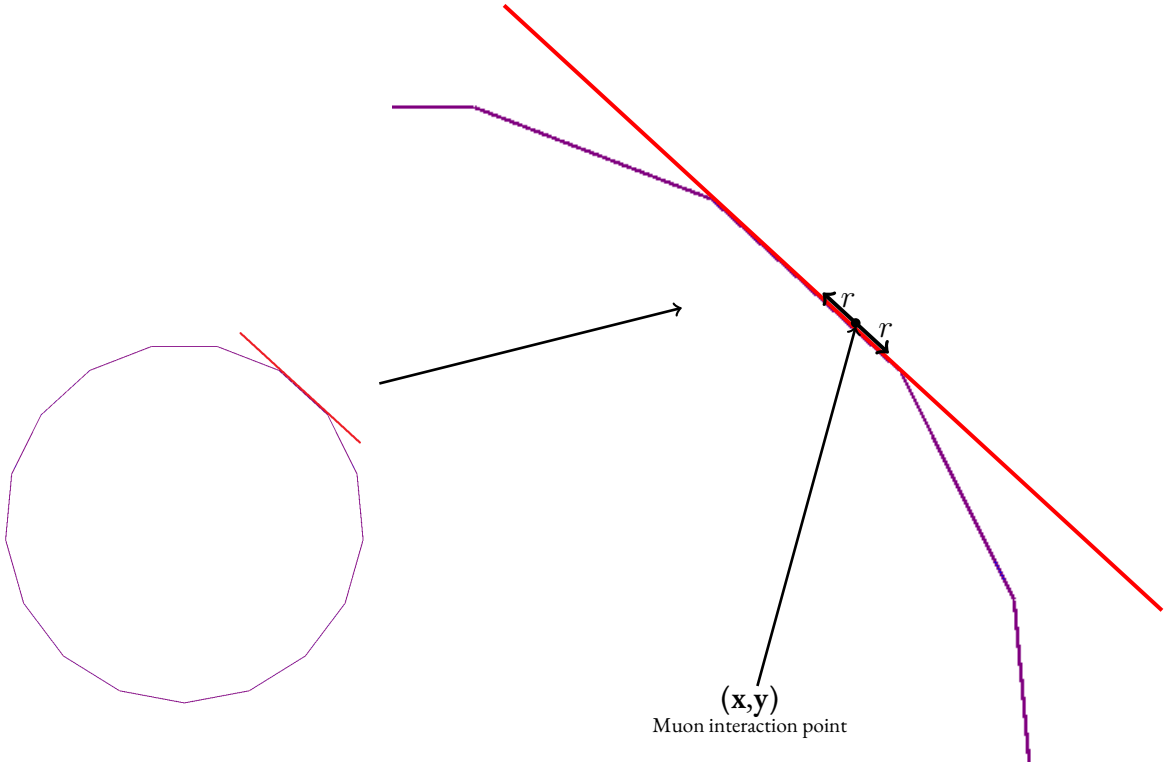

Figure 3.4: Transverse section of one layer of the muon ID (x, y plane), schematic of digitization for the $x - y$ position.

The detector ID provides the information about the required angle of the form,

$$\phi^{'} = n \times \phi \tag{3.11}$$

where n is an integer between and including 0 to 16 and the rotation angle being $-\phi^{'}$. If the muon interaction position or the hit position in gas volume is **(x,y)** rotated coordinates are given by,

$$y^{'} = \mathbf{y}\cos\left(-\phi^{'}\right) - \mathbf{x}\sin\left(-\phi^{'}\right) \tag{3.12}$$

$$x^{'} = \mathbf{x}\cos\left(-\phi^{'}\right) + \mathbf{y}\sin\left(-\phi^{'}\right) \tag{3.13}$$

The value of the $y^{'} \approx 301$ for layer 1 of RPC at the muon ID chamber and 316 for layer 2. Once, the hit or the muon interaction position has been transformed with the vector rotation, the comparison of x-coordinate value with the strip edges of the reference RPC suffices the digitization requirement. Similar to the z axis case, the strips which are within the range of $x^{'} + r$ and $x^{'} - r$ are consider to be charge induced strips and mean of their centre position ($x^{''}$) is calculated. Fi-

nally, the vector formed with the $x^{''}$, $y^{'}$ and $x = 0, y = 0$ is rotated back with the same angle $\phi^{'}$, to get the digitized x, y position.

$$y = y^{'} \cos(\phi^{'}) - x^{''} \sin(\phi^{'}) \tag{3.14}$$

$$x = x^{''} \cos(\phi^{'}) + y^{'} \sin(\phi^{'}) \tag{3.15}$$

The mean can also be found after final rotation of the centre position of the induced strips which are with in the reference RPC followed by temporarily storing them. The algorithm for the digitization along $x - y$ axis has been shown in the Algorithm 2.

In this study the second approach for the digitization along the x, y axis has been considered, which is only possible because there is a symmetry in our geometry and one RPC has been placed perpendicular to a axis (y axis in this study). If we want to simulate the general case, the first method must be taken into account. The simulation in Geant4 provide the hit information in terms of (**x,y,z**). Two sets of random numbers must be generated for two layer of RPCs at the radius of 301 cm (3.01 m) and 316 cm (3.16 m) respectively. It is important to consider the same random number for the digitization of the z axis and x, y axis positions for both layers of RPCs. Thus, the number of hits irrespective of particle in the gas volume of both RPC layers must be same to the generated random number for the particular layer.

If the strips were sensitive instead of the gas volume and the centre position of the fired strips were considered for digitization, the digitized position of the muon hit would have been less accurate because the granularity effect would have been higher (5 cm). The digitization scheme in this study with the gas volume as sensitive would provide better position information. The case when the muon track is close to the edge of the strips, the simulation of the circle will ensure that the corresponding adjacent strip also gets fired or induced and as a result the mean of the centre positions of the fired strips will ensure that the digitized position is close to the gap in between the strips.

Algorithm 2 Digitization scheme for $x - y$-axis

Input: Centre position (x-coordinate), left and right edge (x-coordinate) of all the strips of single RPC positioned along x-axis, random radius r, detector ID (0 to 153), (x, y)-coordinate of the hit position ($(\mathbf{x}, \mathbf{y})$) in the gas volume
Output: Digitized (x, y)-coordinate value.
Create three arrays: `x_plus`, `x_minus`, `x_centre`
for each strip in the bottom layer of particular RPC along x axis only **do**
    Store the x coordinate of edge towards $+x$ axis in `x_plus`
    Edge towards $-x$ axis in `x_minus`
    `x_centre` for centre of the strip, the indices of three should match.
end for
for Hit in the gas volume **do**
    Check the corresponding detector ID and find the integer value n.
    Create an array `x_temp`
    Rotate the position vector **(x,y)** with $-\phi^{'}$ to find $(x^{'}, y^{'})$
    for each strip(indices) in the bottom layer of particular RPC along x axis only **do**
        If `x_minus[index]` $> x^{'} - r$ and `x_plus[index]` $< x^{'} + r$:
            Store the `z_centre[index]` in `z_temp`
        End If
        If `x_minus[index]` $< x^{'} - r$ and `x_plus[index]` $> x^{'} - r$:
            Store the `x_centre[index]` in `z_temp`
        End If
        If `x_minus[index]` $< x^{'} + r$ and `x_plus[index]` $> x^{'} + r$:
            Store the `x_centre[index]` in `x_temp`
        End If
    end for
    for Values in `x_temp`
        Rotate back values,$y^{'}$ with $\phi^{'}$, store in arrays `x_temp_digit` and `y_temp_digit`
    end for
        `digit_x`= Mean of the elements in `x_temp_digit`
        `digit_y`= Mean of the elements in `y_temp_digit`
    Return `digit_x`, `digit_y`
end for

3.3 Muon path reconstruction with non-magnetic absorber

The muon path reconstruction in the non-magnetic absorber case is shown in Algorithm 3 and Algorithm 4 and illustrated in Figure 3.5.

Algorithm 3 Muon Identification Algorithm

Input: Hits on the false sensitive layer at 2.19 cm (see Figure 3.5)
Output: Identified muons
for each μ hit on the sensitive layer **do**
    Find the momentum a step before the hit
    Find the unit vectors of the momentum along x, y, z
    Extrapolate along the found unit vectors to find hit positions on the strip layers of RPC
    Find the closest hit to the extrapolated hit position
    if closest hit position is within the matching window and PID matched with muon **then**
        Consider it as a μ hit on RPC.
    end if
end for

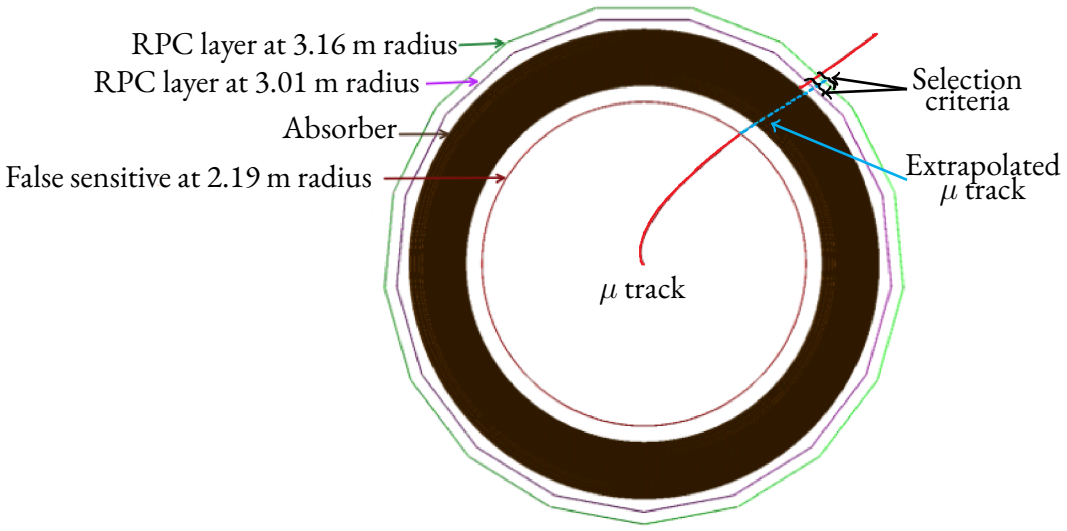

Figure 3.5: Schematic of the extrapolation algorithm.

Algorithm 4 Selection criteria (Matching Window) Calculation

1: **Input:** Extrapolated hits positions, real hit positions on the strips
2: **Output:** Matching window parameters
3: **for** each extrapolated hit position **do**
4: Calculate η and ϕ for extrapolated x, y, z
5: Calculate η and ϕ for each hit(irrespective of particle) on the strips
6: For each hit calculate $\Delta\eta = \eta_{\text{extrapolated}} - \eta_{\text{hit}}$, $\Delta\phi = \phi_{\text{extrapolated}} - \phi_{\text{hit}}$
7: Fill a 2D histogram with closest $\Delta\eta$ and $\Delta\phi$ (which will be for each μ at the sensitive layer)
8: **end for**
9: Fit the histogram with a Gaussian function after projecting the $\Delta\eta$ and $\Delta\phi$ to one dimension to obtain $\sigma_{\Delta\eta}$ and $\sigma_{\Delta\phi}$

The reconstruction in this study will focus on the muon track at a radius less than the absober and extended till the muon ID chamber. To implement that there is a false sensitive layer at 219 cm. The information of the particle hitting this layer is collected as the reference which include particle ID, momentum, hit position. The non-magnetic absrober case has the benefit of linear extrapolation with the momentum information from this layer. For a muon hit in this layer, the unit vector along that momentum is found and extrapolated with respect to that unit vector till both the layers of the muon ID chamber. If a muon hit is found within a matching window of the extrapolated muon track, it is consider that the muon is detected for the corresponding muon hit in the sensitive layer at 219 cm. The matching window or the selection criteria for the detection of muon which is describe in Algorithm 4. To find the selection criteria, the muon path hitting the sensitive layer is extrapolated to the muon ID and the extrapolated position is found in the $\eta - \phi$ coordinate. The differences between a extrapolated position and all hit position irrespective of particles are filled in a two dimensional histogram. The histogram is fitted with a Gaussian function after projecting axis in one dimension for both the η and ϕ axes. The selection criteria is p_T dependent, for $p_T < 2$ GeV/c the selection criteria is $1 \times \sigma$ or the variance of the fitted Gaussian function and $p_T > 2$ Gev/c the selection criteria is $2 \times \sigma$ or twice the variance of the fitted Gaussian function. For the extrapolation of the muon track the extrapolated position will be very close to the muon hit (the differences between extrapolated and hit positions are close to 0) and for the other particle it will be randomly distributed (the differences between extrapolated and hit positions are random). Thus, the difference of the hit and extrapolated position which fill the two dimensional histogram for all the muon hits in the sensitive layer will be Gaussian according to the *central limit theorem*.

3.4 Muon path reconstruction with magnetic absorber

To reconstruct the muon path for the magnetic absorber case the extrapolation algorithm has to be modified. We have to simulate the relativistic path of a charged particle though a static magnetic field, which is helix. The simulation toolkit Geant-4 propagates the particle while simultaneously solving the coupled differential equation for the resulting Lorentz force. It employs the Runge-Kutta 4 numerical method.

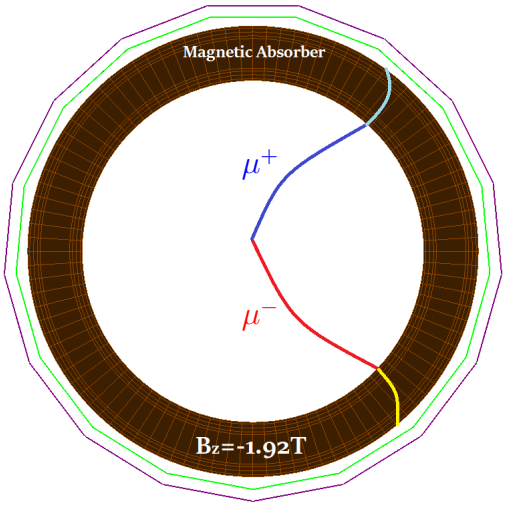

Figure 3.6: Schematic of the muon track in the magnetic absorber.

We know the Lorentz equation for a charged particle in a magnetic field is given by,

$$\frac{d\vec{p}}{dt} = q\vec{v} \times \vec{B} \tag{3.16}$$

The vector $\vec{p}$ is the relativistic momentum, $\vec{v}$ is the velocity and the vector $\vec{B}$ is the magnetic field vector and q is the charge of the particle. This can be simplified as,

$$\gamma m \left(\frac{d\vec{v}}{dt}\right) = q\vec{v} \times \vec{B} \tag{3.17}$$

γ is the Lorentz factor given by,

$$\gamma = \sqrt{\frac{1}{1 - (\frac{v}{c})^2}} \tag{3.18}$$

where v is the modulus of the velocity vector and c is the speed of light. In the differential equation we have $\vec{v}$ as a variable, but because the field is static the Lorentz force just changes the direction of the velocity and not its modulus value which remains constant. This can also be argued by the fact that the energy of the complete system is conserved, the γ **is constant**.

$$\frac{d\vec{v}}{dt} = \frac{q}{\gamma m}\vec{v} \times \vec{B} \tag{3.19}$$

consider,

$$\omega = \frac{q}{\gamma m} \tag{3.20}$$

$$\frac{d\vec{v}}{dt} = \omega\vec{v} \times \vec{B} \tag{3.21}$$

The magnetic field is only along the z axis which is given as,

$$\vec{B} = B_z\hat{k} \tag{3.22}$$

So we can rewrite the equations as,

$$\frac{dv_x}{dt} = \omega v_y B_z \tag{3.23}$$

$$\frac{dv_y}{dt} = -\omega v_x B_z \tag{3.24}$$

$$\frac{dv_z}{dt} = 0 \tag{3.25}$$

consider,

$$\omega B_z = \omega_c \tag{3.26}$$

$$\frac{dv_x}{dt} = \omega_c v_y, \frac{dv_y}{dt} = -\omega_c v_x, \frac{dv_z}{dt} = 0 \tag{3.27}$$

If we replace v_y in the equation 3.24 from the equation 3.23, we get,

$$\frac{d}{dt}\left(\frac{dv_x}{dt}\right) = -\omega_c^2 v_x \tag{3.28}$$

$$\frac{d^2 v_x}{dt^2} = -\omega_c^2 v_x \tag{3.29}$$

The equation 3.29 is the oscillator equation and we know the general solution to that is given by,

$$v_x = P\cos(\omega_c t) + Q\sin(\omega_c t) \tag{3.30}$$

where P and Q are constants. Now, at t=0,

$$v_x(t=0) = P = v_{x,0} \tag{3.31}$$

If we take the derivative of v_x with respect to t and divide by ω_c, we get,

$$v_y = -v_{x,0}\sin(\omega_c t) + Q\cos(\omega_c t) \tag{3.32}$$

At $t = 0$,

$$v_y(t=0) = Q = v_{y,0} \tag{3.33}$$

So, we get the solution of the equation as,

$$v_x = v_{x,0}\cos(\omega_c t) + v_{y,0}\sin(\omega_c t) \tag{3.34}$$

$$v_y = -v_{x,0}\sin(\omega_c t) + v_{y,0}\cos(\omega_c t) \tag{3.35}$$

$$v_z = v_z \tag{3.36}$$

Now, to find the position we integrate the functions over the time 0 to T,

$$x(t=T) = \int_0^T v_x dt \tag{3.37}$$
$$= \frac{1}{\omega_c} \{v_{x,0} \sin(\omega_c t) - v_{y,0} \cos(\omega_c t)\} \,|_0^T + x(t=0) \tag{3.38}$$
$$= \frac{1}{\omega_c} [v_{x,0} \sin(\omega_c T) + v_{y,0}\{1 - \cos(\omega_c T)\}] + x(0) \tag{3.39}$$

similarly,

$$y(t=T) = \int_0^T v_y dt \tag{3.40}$$
$$= \frac{1}{\omega_c} \{v_{x,0} \cos(\omega_c t) + v_{y,0} \sin(\omega_c t)\} \,|_0^T + y(t=0) \tag{3.41}$$
$$= \frac{1}{\omega_c} [v_{x,0}\{\cos(\omega_c T) - 1\} + v_{y,0} \sin(\omega_c T)] + y(0) \tag{3.42}$$

and finally,

$$z(t=T) = z(t=0) + v_{z,0}T = z(0) + v_{z,0}T \tag{3.43}$$

$$v_x(T) = v_{x,0} \cos(\omega_c T) + v_{y,0} \sin(\omega_c T) \tag{3.44}$$
$$v_y(T) = -v_{x,0} \sin(\omega_c T) + v_{y,0} \cos(\omega_c T) \tag{3.45}$$
$$v_z(T) = v_z \tag{3.46}$$

$$x(T) = \frac{1}{\omega_c} [v_{x,0} \sin(\omega_c T) + v_{y,0}\{1 - \cos(\omega_c T)\}] + x(0) \tag{3.47}$$
$$y(T) = \frac{1}{\omega_c} [v_{x,0}\{\cos(\omega_c T) - 1\} + v_{y,0} \sin(\omega_c T)] + y(0) \tag{3.48}$$
$$z(T) = v_{z,0}T + z(0) \tag{3.49}$$

The point to be noted is that here we are considering the ideal path of the charged particle in the magnetic field which will not be the case for the muon in the magnetic absorber. As mentioned earlier, the change in energy with respect to time is constant but the muon while traversing

the path inside the absorber will experience energy loss. We have neglected the energy loss though Geant-4 takes that into account. This loss in energy will deviate the path further with increase in curvature. We expect that effect in the $\Delta\phi$ value for the magnetic case even if we try to find the extrapolated position with simulating the helical path. The rest of the algorithm remains the same as earlier to the Algorithm 3 and Algorithm 4 with only modification in the extrapolation.

3.5 Performance of the RPC based muon ID chamber

The performance of the simulated RPC based muon ID chamber is studied with muon detection efficiency and J/ψ reconstruction efficiency. The muon detection efficiency is defined as,

$$\epsilon = \frac{\text{detected muon in the muon ID chamber}}{\text{muon hit on the false sensitive layer}} \tag{3.50}$$

For a muon track to be considered as detected, it must hit both the layers of the muon ID chamber and is within the selection criteria. The muon hits are confirmed with the monte carlo particle ID [16] as well. The error in the efficiency is estimated with Poisson error[17]. The error is given by,

$$\delta\epsilon_i = \epsilon_i \sqrt{\left(\frac{\delta k_i}{k_i}\right)^2 + \left(\frac{\delta N_i}{N_i}\right)^2} \tag{3.51}$$

where ϵ_i is the efficiency for a bin in the efficiency histogram, which is defined as,

$$\epsilon_i = \frac{k_i}{N_i} \tag{3.52}$$

$$\epsilon = \frac{k}{N}\left(\frac{1}{k} + \frac{1}{N}\right) \tag{3.53}$$

$$\epsilon = \sqrt{\frac{k^2(N+k)}{k^3}} \tag{3.54}$$

The J/ψ reconstruction efficiency is found with invariant mass of the detected μ^+ and μ^- for the dimuon decay channel of J/ψ given by,

$$m^2_{J/\psi} = (p^0_{\mu^+} + p^0_{\mu^-})^2 - (\vec{p}_{\mu^+} + \vec{p}_{\mu^-})^2 \tag{3.55}$$

where p^0 is the energy term of the 4-$momentum$. The energy can be written as,

$$p^0 = \sqrt{m_\mu^2 + p_\mu^2} \tag{3.56}$$

where m_μ is the rest mass of muon. Therefore the momonetum information is enough to find the invariant mass of $\mu^+\mu^-$.

Chapter 4

Results of simulated muon ID chamber

η and ϕ matching window selection for μ hit with non-magnetic absorber for pp collisions

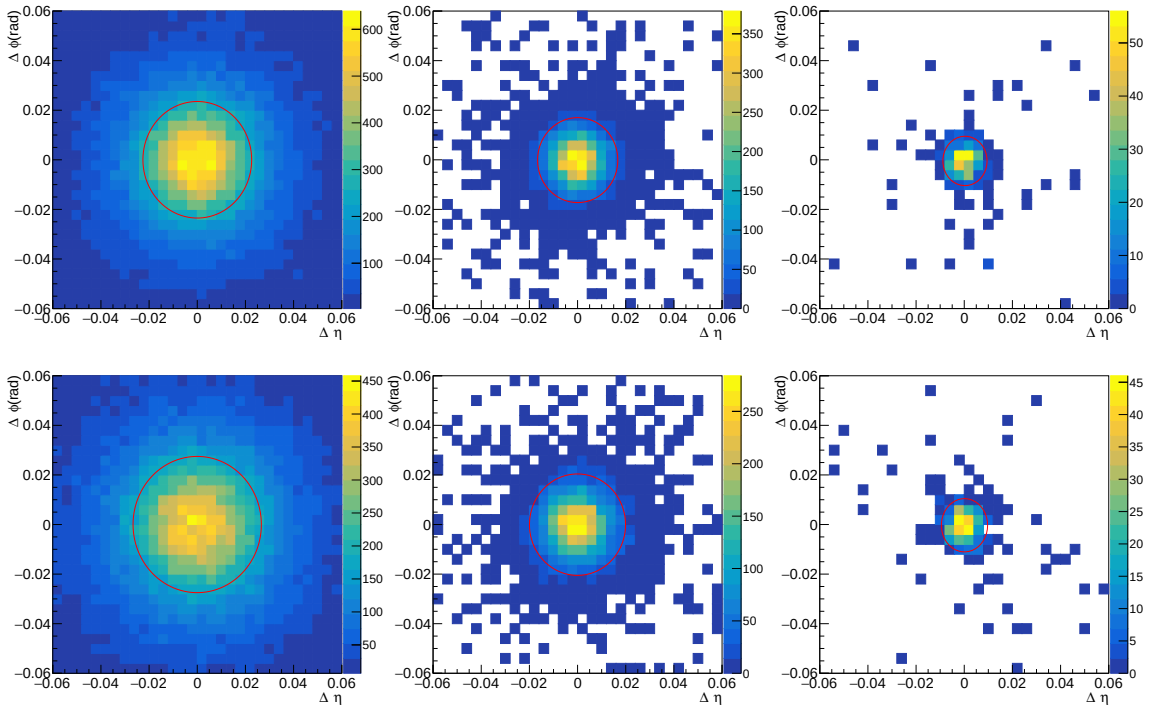

(a) $p_T < 2$GeV/c (b) $2 < p_T < 5$GeV/c (c) $p_T > 5$GeV/c

Figure 4.1: $\Delta\eta$ and $\Delta\phi$ matching window for pp collisions with non-magnetic absrober. The rows show RPC Layer 1 and 2 for the RPC at 3.01 m radius (top row) and at 3.16 m radius (bottom row) for the 3 different p_T range in the columns. The selection cuts for various layers shown in red color ellipse.

Layer	$p_T < 2$ **GeV**/c	$2 < p_T < 5$ **GeV**/c	$5 < p_T < 10$ **GeV**/c
RPC layer 1	$\sigma_{\Delta\eta} = 0.0226$	$2\sigma_{\Delta\eta} = 2 \times 0.0083$	$2\sigma_{\Delta\eta} = 2 \times 0.0046$
(Radius 3.01 m)	$\sigma_{\Delta\phi} = 0.0235$	$2\sigma_{\Delta\phi} = 2 \times 0.0086$	$2\sigma_{\Delta\phi} = 2 \times 0.0050$
RPC layer 2	$\sigma_{\Delta\eta} = 0.0266$	$2\sigma_{\Delta\eta} = 2 \times 0.0010$	$2\sigma_{\Delta\eta} = 2 \times 0.0048$
(Radius 3.16 m)	$\sigma_{\Delta\phi} = 0.0275$	$2\sigma_{\Delta\phi} = 2 \times 0.0102$	$2\sigma_{\Delta\phi} = 2 \times 0.0054$

Table 4.1: $\Delta\eta$-$\Delta\phi$ selection criteria (matching window) for pp collisions with non-magnetic absorber.

η and ϕ matching window selection for μ hit with Magnetic absorber for pp collisions

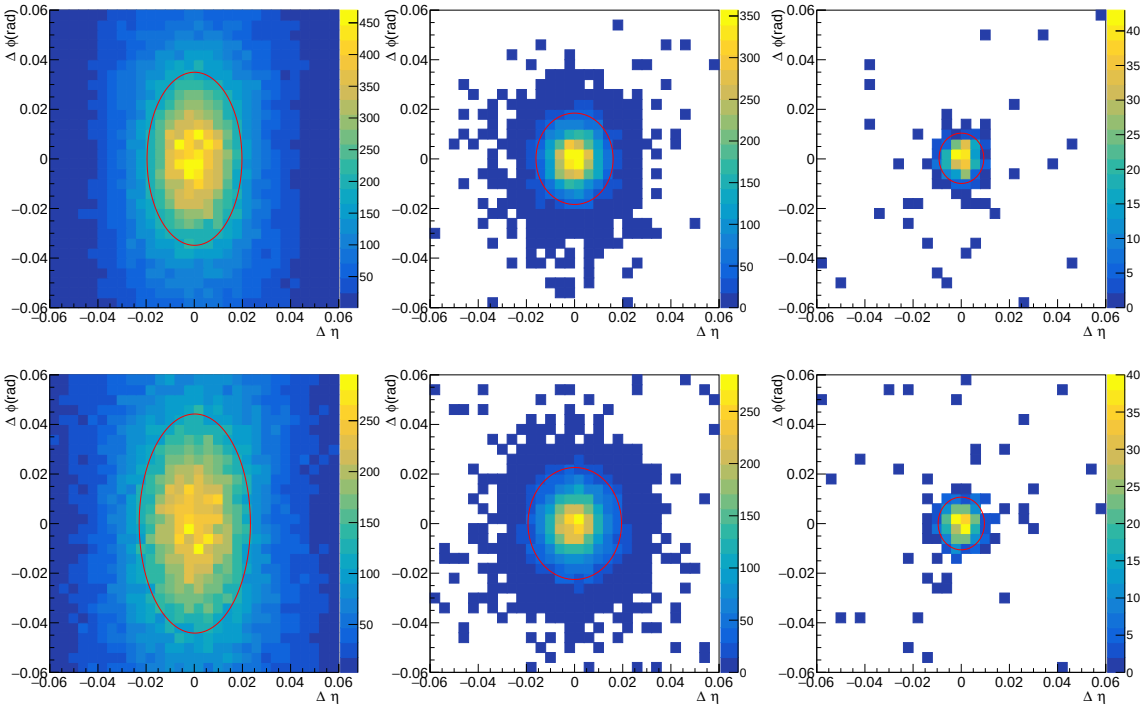

(a) $p_T < 2$GeV/c (b) $2 < p_T < 5$GeV/c (c) $p_T > 5$GeV/c

Figure 4.2: $\Delta\eta$ and $\Delta\phi$ matching window for pp collisions with magnetic absrober. The rows show RPC Layer 1 and 2 for the RPC at 3.01 m radius (top row) and at 3.16 m radius (bottom row) for the 3 different p_T range in the columns. The selection cuts for various layers shown in red color ellipse.

Layer	$p_T < 2$ **GeV**/c	$2 < p_T < 5$ **GeV**/c	$5 < p_T < 10$ **GeV**/c
RPC layer 1	$\sigma_{\Delta\eta} = 0.0197$	$2\sigma_{\Delta\eta} = 2 \times 0.0080$	$2\sigma_{\Delta\eta} = 2 \times 0.0047$
(Radius 3.01 m)	$\sigma_{\Delta\phi} = 0.0349$	$2\sigma_{\Delta\phi} = 2 \times 0.0092$	$2\sigma_{\Delta\phi} = 2 \times 0.0051$
RPC layer 2	$\sigma_{\Delta\eta} = 0.0231$	$2\sigma_{\Delta\eta} = 2 \times 0.0097$	$2\sigma_{\Delta\eta} = 2 \times 0.0048$
(Radius 3.16 m)	$\sigma_{\Delta\phi} = 0.0442$	$2\sigma_{\Delta\phi} = 2 \times 0.0113$	$2\sigma_{\Delta\phi} = 2 \times 0.0053$

Table 4.2: $\Delta\eta$-$\Delta\phi$ selection criteria (matching window) for pp collisions with magnetic absorber.

The figures were generated with CERN ROOT with simulated data from Pythia and Geant-4. The three columns show the $\Delta\eta$(on the x axis) and $\Delta\phi$(on the y axis) distributions for the muon hits with respect to all the hits for the different p_T range while the rows illustrate the distribution for the 2 RPC layers. The red color ellipse shows the range of $\Delta\eta$ and $\Delta\phi$ that we have selected as our μ detection matching window or the selection criteria, this selection is p_T dependent as stated before.
The σ values were obtained after projecting the η and the ϕ to the suitable range in one dimension and then fitting them with a Gaussian function.

In the Figure 4.1 The matching window selection for the η and ϕ are given. The effect of granularity due to the digitization of the strips have been taken into account. Better position information can be obtained with reduction of strip width but that will give rise to the electronics component in the setup.

In the Figure 4.2 the $\Delta\eta$ and $\Delta\phi$ matching window for the magnetic absorder case is shown. The y axis of the plots are in terms of $\Delta\phi$. We see the effect of the magnetic absorber on the charged particles on the $\Delta\phi$ resulting in higher value of $\Delta\phi$ as discussed earlier regarding the energy loss in the absorber. Therefore the extrapolation with estimating the energy loss in the absorber will have better position information on the muon ID chamber. The magnetic field inside the absorber is in the z direction and thus we do not see any change in the η because η depends on the $\sqrt{x^2 + y^2}$ (that is constant with respect to the position of the RPC layers which is basically their radius) and the z which is also unaffected by the magnetic field.

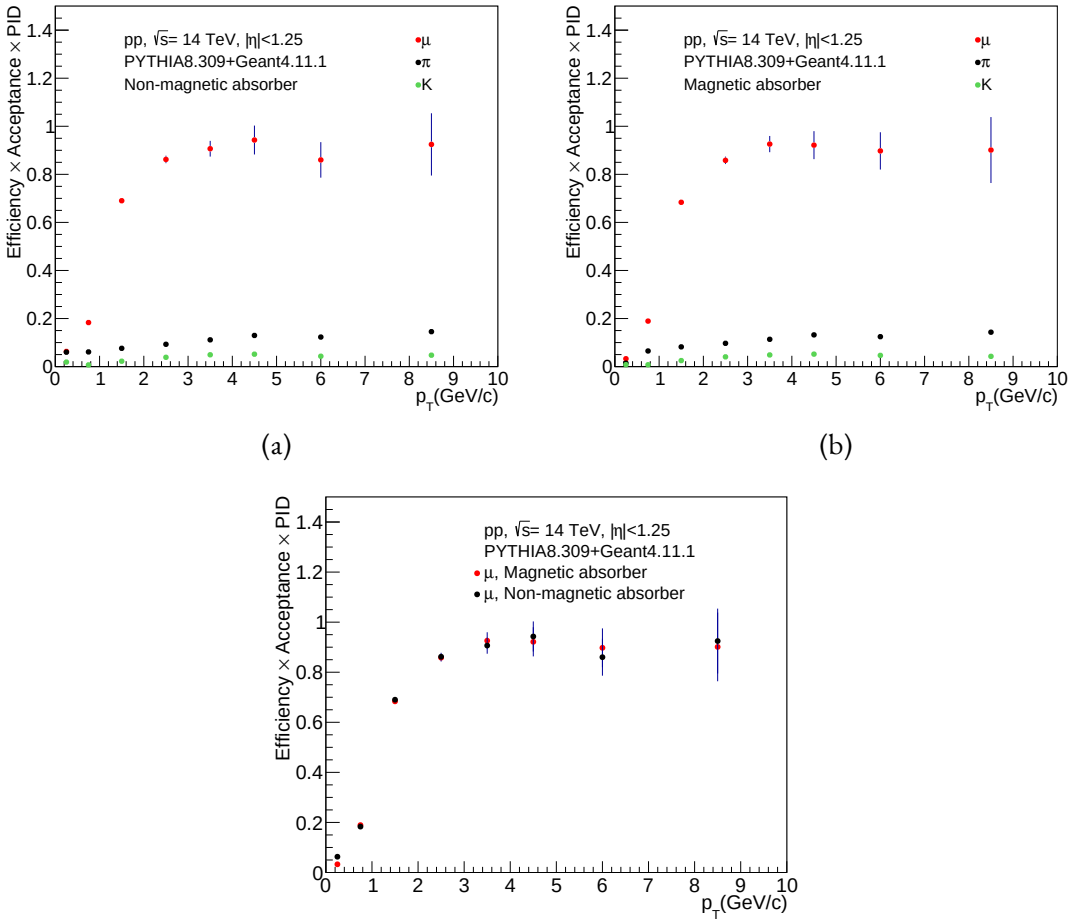

Figure 4.3: (a)μ(in red) detection efficiency with π(in black) & K(in green) background with non-magnetic absorber, (b) μ(in red) detection efficiency with π(in black) & K(in green) background with magnetic absorber, (c) Comparison of μ detection efficiency with magnetic (Red) and non-magnetic absorber (black).

In the Figure 4.3 the magnetic and non-magnetic absorber study of efficiency for muon (in red) detection and pion (in black) and kaon (in green) detection are shown (pion and kaon are backgrounds). In the plots, the x axis is the transverse momentum (p_T) and y axis is the efficiency of particle detection. One more factor is included which is acceptance,the η-pseudorapidity selection along with the Particle ID (PID) of detected particle.

In Figure 4.3a and 4.3b, we can see that, at $p_T > 1.5$ GeV/c efficiency of muon (marker in red) detection for the magnetic and the non-magnetic case is close to 90%. For the pion (points

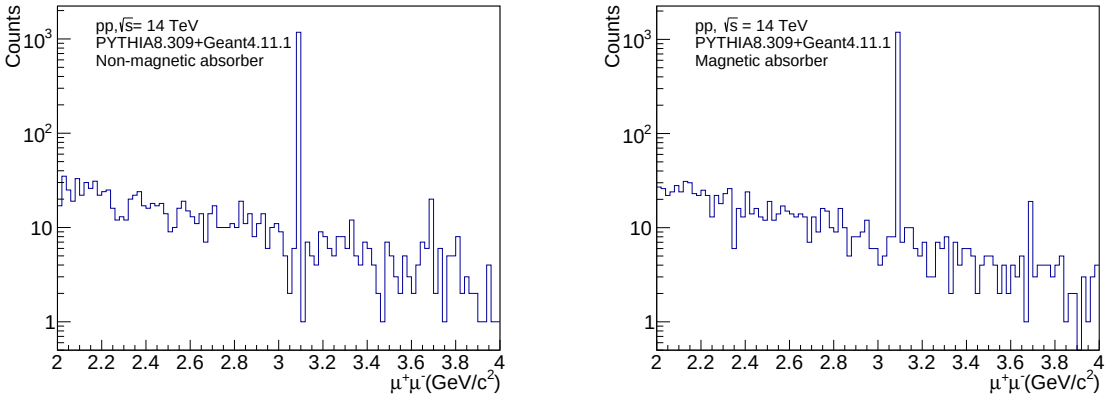

(a) (b)

Figure 4.4: (a)$\mu^+\mu^-$ invariant mass reconstruction with non-magnetic absorber, (b) $\mu^+\mu^-$ invariant mass reconstruction with magnetic absorber.

in black) and kaon (points in green), the efficiencies are less than 10% till 2 GeV/c. The maximum background is from the pion with the highest found efficiency to be 14%. The error bars on the result are statistical error. The errors are higher at higher transverse momentum because the particle count is low in the higher transverse momentum range.

The Figure 4.3c shows the comparison of the muon detection efficiency for the magnetic and the non-magnetic absorber case, it is evident that the absrober choice has no effect on the muon detection efficiency.

Figure 4.4 illustrates the reconstructed invariant mass of the detected μ^+ and μ^- particles with the selection criteria and with in the acceptance $|\eta| < 1.25$, for two million pp collision events with both non-magnetic and magnetic absorbers. A prominent peak appears around 3.1 GeV/c^2, corresponding to the mass of the J/ψ particle which is a charmonium. Since the stored momentum originates from the generator level, a single peak is observed at a specific value.

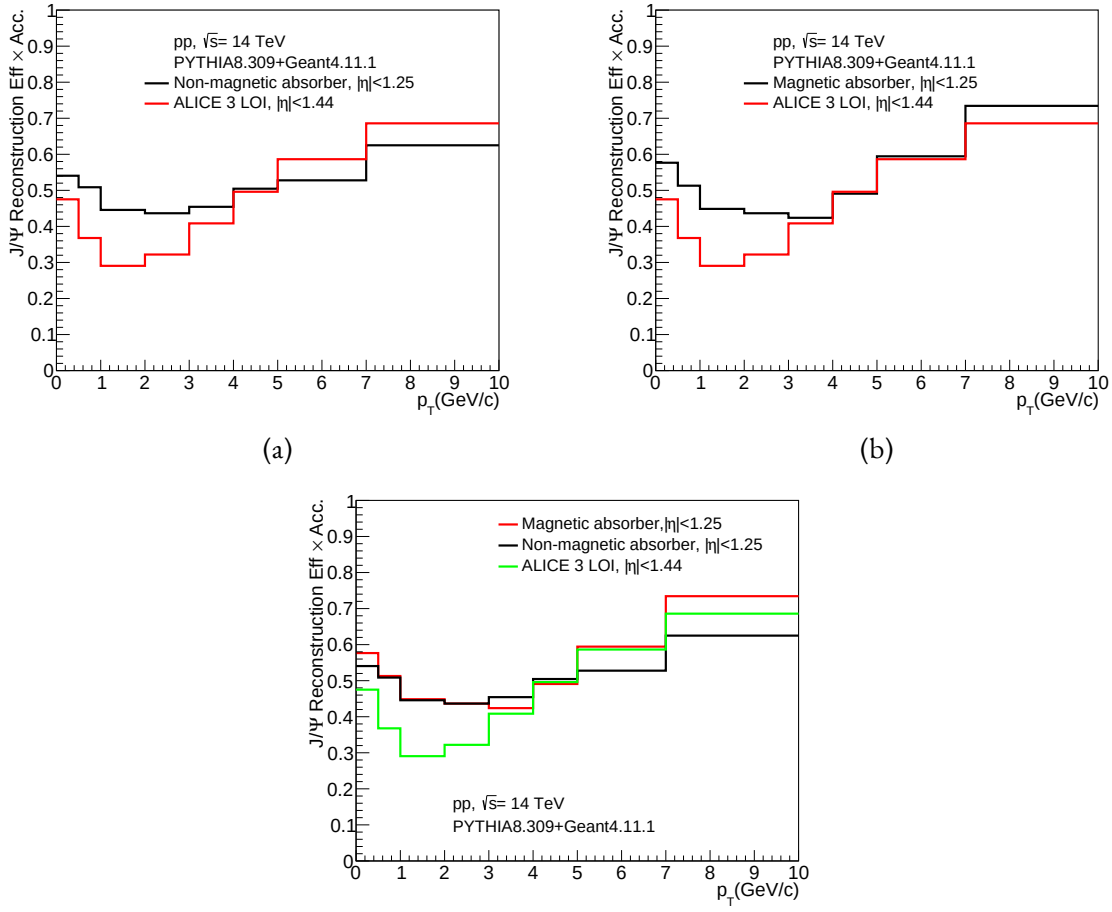

Figure 4.5: (a) J/ψ reconstruction efficiency for the non-magnetic absorber, our study in black and LOI in red and, (b) J/ψ reconstruction efficiency for the magnetic absorber ,our study in black and LOI in red, (c) J/ψ reconstruction efficiency, LOI in green and our study for magnetic absorber in red and non-magnetic absrober in black.

In the Figure 4.5, J/ψ reconstruction efficiency is calculated with the J/ψ reconstructed with the detected muon and the generated dimuon which are also reconstructed to get J/ψ with the acceptable η range. Therefore J/ψ reconstruction efficiency is the ratio of J/ψ reconstructed to the J/ψ generated and decaying with dimuon channel. In the ALICE3 LOI, plastic scintillators and non-magnetic absorber were considered. We have performed simulations for both cases of absorbers but with the RPC based geometry. J/ψ reconstruction efficiency in our study is appearing to be better compared to the LOI calculations. This may be due to the fact we used a geometry different to what was used in the LOI (RPC vs. Plastic scintillator). The choice of absorber material have minimal effect for J/ψ reconstruction efficiency with low p_T.

η and ϕ matching window selection for μ hit with non-magnetic absorber for $Pb-Pb$ collisions

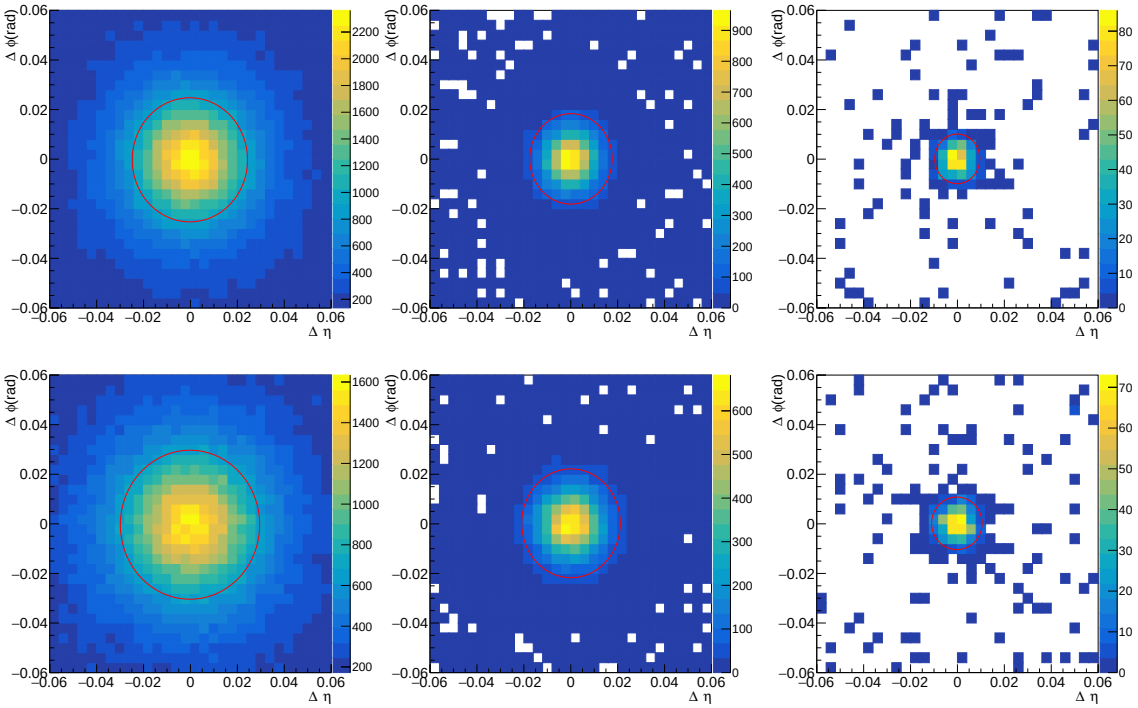

(a) $p_T < 2$GeV/c (b) $2 < p_T < 5$GeV/c (c) $p_T > 5$GeV/c

Figure 4.6: $\Delta\eta$ and $\Delta\phi$ matching window for Pb-Pb collisions with non-magnetic absrober. The rows show RPC Layer 1 and 2 for the RPC at 3.01 m radius (top row) and at 3.16 m radius (bottom row) for the 3 different p_T range in the columns. The selection cuts for various layers shown in red color ellipse.

Layer	$p_T < 2$ **GeV**/c	$2 < p_T < 5$ **GeV**/c	$5 < p_T < 10$ **GeV**/c
RPC layer 1	$\sigma_{\Delta\eta} = 0.0246$	$2\sigma_{\Delta\eta} = 2 \times 0.0088$	$2\sigma_{\Delta\eta} = 2 \times 0.0048$
(Radius 3.01 m)	$\sigma_{\Delta\phi} = 0.0250$	$2\sigma_{\Delta\phi} = 2 \times 0.0091$	$2\sigma_{\Delta\phi} = 2 \times 0.0050$
RPC layer 2	$\sigma_{\Delta\eta} = 0.0297$	$2\sigma_{\Delta\eta} = 2 \times 0.0105$	$2\sigma_{\Delta\eta} = 2 \times 0.0054$
(Radius 3.16 m)	$\sigma_{\Delta\phi} = 0.0301$	$2\sigma_{\Delta\phi} = 2 \times 0.0110$	$2\sigma_{\Delta\phi} = 2 \times 0.0053$

Table 4.3: $\Delta\eta$-$\Delta\phi$ selection criteria (matching window) for Pb-Pb collisions with non-magnetic absorber.

η and ϕ matching window selection for μ hit with Magnetic absorber for $Pb-Pb$ collisions

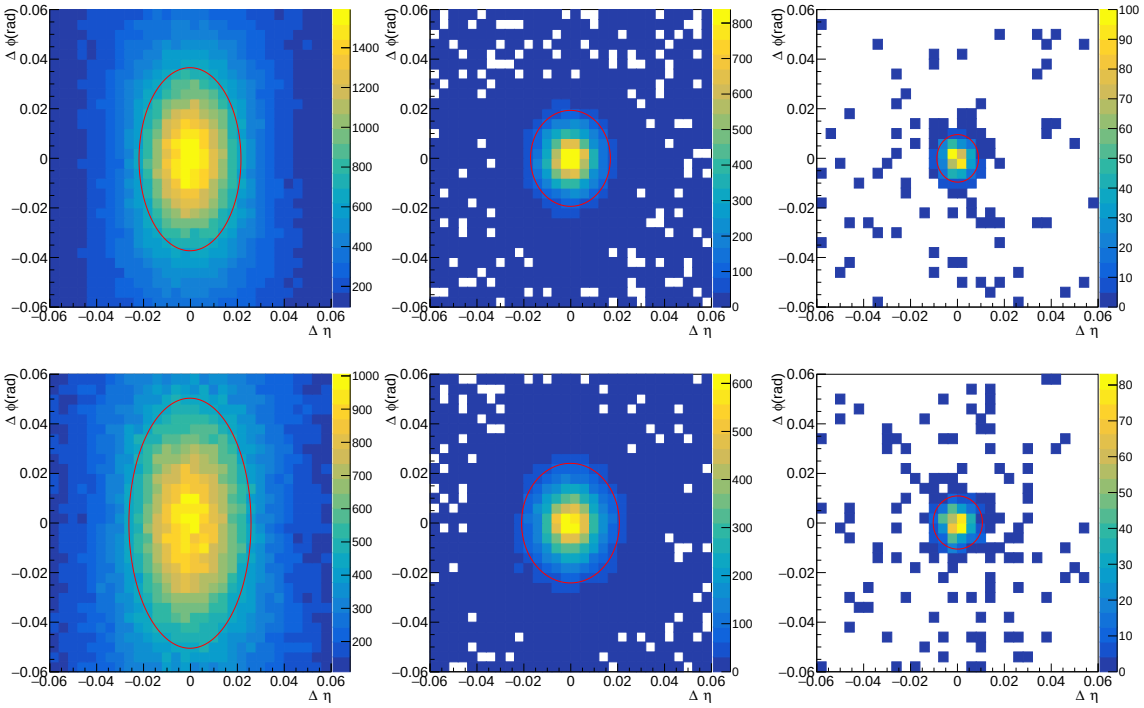

(a) $p_T < 2$GeV/c (b) $2 < p_T < 5$GeV/c (c) $p_T > 5$GeV/c

Figure 4.7: RPC $\Delta\eta$ and $\Delta\phi$ matching window for Pb-Pb collisions with magnetic absrober. The rows show RPC Layer 1 and 2 for the RPC at 3.01 m radius (top row) and at 3.16 m radius (bottom row) for the 3 different p_T range in the columns. The selection cuts for various layers shown in red color ellipse.

Layer	$p_T < 2$ **GeV**/c	$2 < p_T < 5$ **GeV**/c	$5 < p_T < 10$ **GeV**/c
RPC layer 1	$\sigma_{\Delta\eta} = 0.0217$	$2\sigma_{\Delta\eta} = 2 \times 0.0085$	$2\sigma_{\Delta\eta} = 2 \times 0.0045$
(Radius 3.01 m)	$\sigma_{\Delta\phi} = 0.0369$	$2\sigma_{\Delta\phi} = 2 \times 0.0097$	$2\sigma_{\Delta\phi} = 2 \times 0.0048$
RPC layer 2	$\sigma_{\Delta\eta} = 0.0260$	$2\sigma_{\Delta\eta} = 2 \times 0.0104$	$2\sigma_{\Delta\eta} = 2 \times 0.0053$
(Radius 3.16 m)	$\sigma_{\Delta\phi} = 0.0504$	$2\sigma_{\Delta\phi} = 2 \times 0.0121$	$2\sigma_{\Delta\phi} = 2 \times 0.0054$

Table 4.4: $\Delta\eta$-$\Delta\phi$ selection criteria (matching window) for Pb-Pb collisions with magnetic absorber.

The Figure 4.6 and 4.7 shows the $\Delta\eta$ and $\Delta\phi$ distribution as 2D histogram for non-magnetic and the magnetic absorber case respectively for Pb-Pb collisions, with the similar method for the

pp collisions case.The y axis is the $\Delta\phi$ and x is the $\Delta\eta$ and the red ellipse shows the matching window for the μ selection. The transverse momentum condition remains the same as it was for the pp collision case, 1σ for $p_T < 2$ Gev/c, 2σ for $p_T > 2$ Gev/c. The $\Delta\phi$ selection for the magnetic absorber case is quite high. This is due to the same reason of energy loss of the muon in the absorber which bends the muon path further in the absorber.

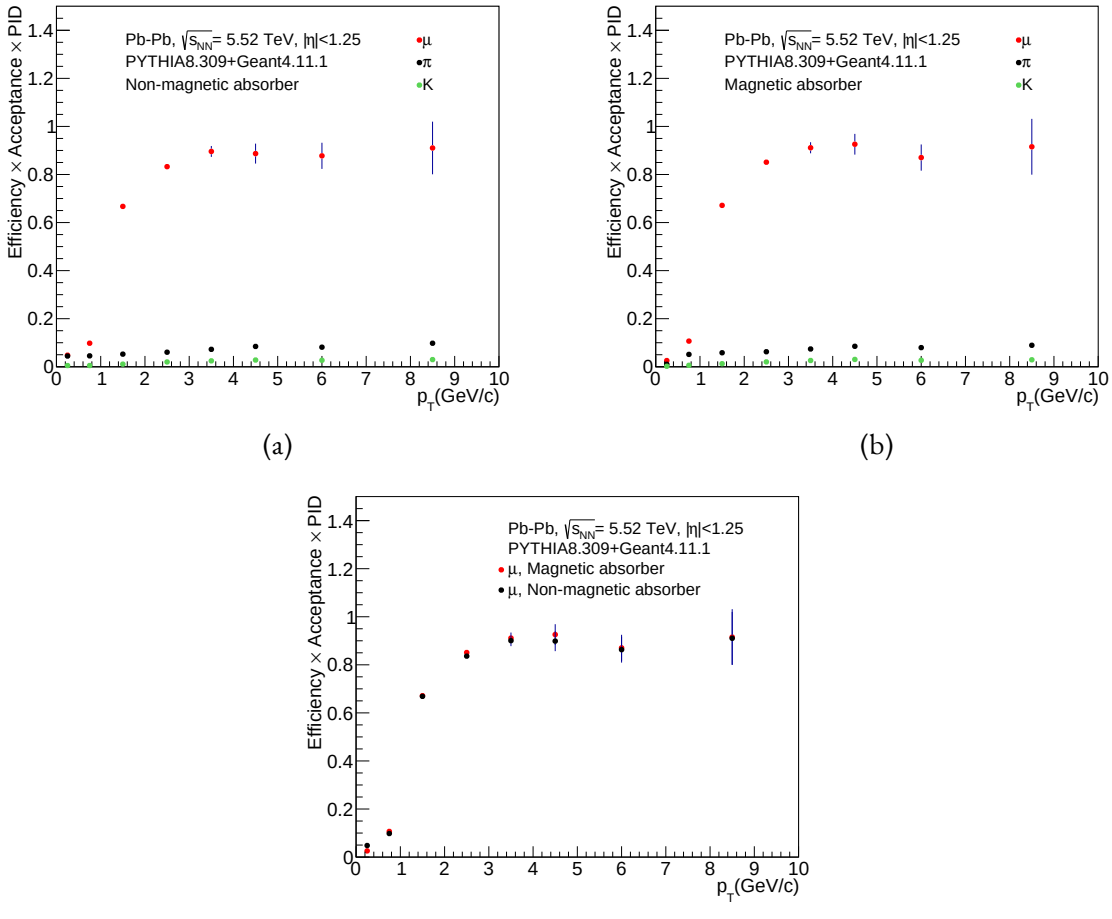

Figure 4.8: (a)μ(in red) detection efficiency with π(in black) & K(in green) background with non-magnetic absorber, (b) μ(in red) detection efficiency with π(in black) & K(in green) background with magnetic absorber, (c) comparison of the muon detection efficiency with the magnetic and the non-magnetic absorber case.

The muon detection efficiency for the Pb-Pb collisions has been shown in Figure 4.8 along with the background π and K. The muon detection efficiency is more than 90% at $p_T > 2$ GeV/c and the background efficiency is $\sim$ 10%. The absorber choice has no effect on the muon

detection efficiency even for the Pb-Pb collisions as well which is evident from the Figure 4.8c.

Chapter 5

Development of Hybrid RPC

RPCs are gas based detectors. They are operated at very high voltages with standard operating gases R134A and SF_6 which are green house gases with very high green house potential. To mitigate the use of green house gas in the operation of RPCs we can have two approaches, which are following,

- Make hardware modification which can work with low gas flow rate.
- Make use of eco-friendly gases without compromising the detection efficiency and resolution.

An attempt to the first approach has been made with a proposed hybrid detector [6]. The design for that RPC is with one metal electrode plate of size $9\times9\,cm^2$. The other electrode is glass coated with conductive paint(Graphite). The metal electrode is coated with metal oxides which have the property of secondary electron multiplication. These two electrodes were used to make the RPC chamber and the metal electrode itself worked as the readout. The RPC was tested with R134A and SF_6 and iso-butane but with a gas flow rate of 2-3 scc/min where as usual gas flow rate for RPC is 5-6 scc/min.

We have build a hybrid RPC with a new geometry with two gas gaps. The design is shown in the Figure 5.1.

There are two glass electrodes of thickness 3 mm and size $20\times20\,cm^2$ coated with conductive paint. The conductive paint we have used is graphite which is mixed with thinner and coated on the glass plate with an air brush. The resulting surface resistivity of the glass is $\sim1\,M\Omega/\square$ with the graphite covering the area of $17\times17\,cm^2$.

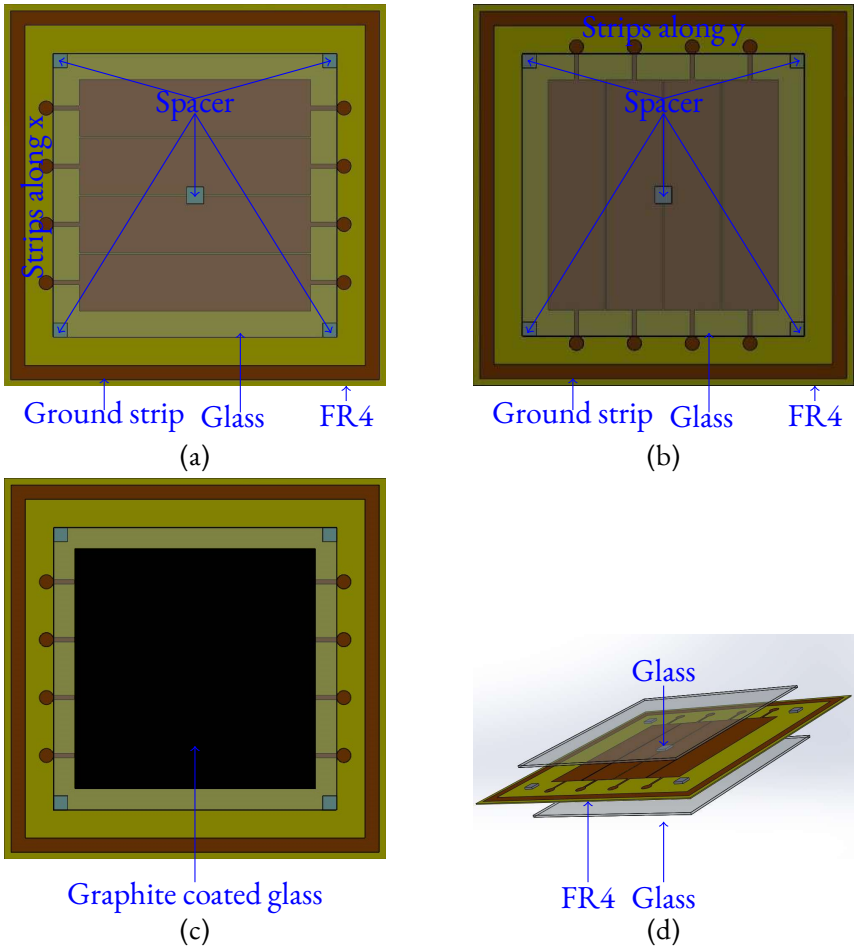

Figure 5.1: (a) Model from top along positive z (b) Model from top along negative z (c)Top view with graphite coated glass (d) exploded view of the model.

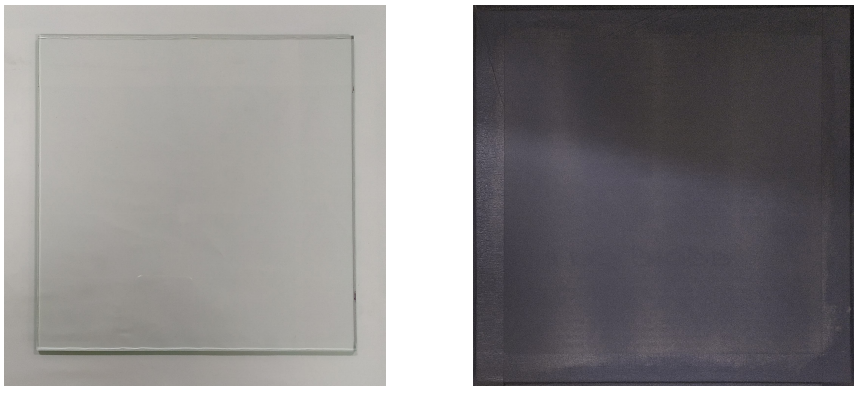

Figure 5.2: Glass electrode (a) before graphite coating and (b) after coating with graphite.

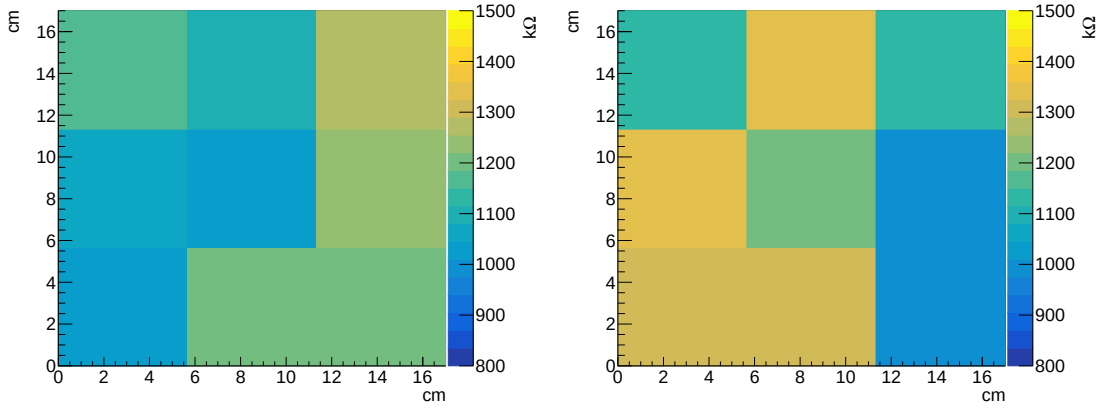

(a) (b)

Figure 5.3: Glass electrode surface resistivity after graphite coating kΩ/□ (a) glass layer on top (b) glass layer at bottom.

In the Figure 5.3, the surface resistivity of the graphite coated glass plates are shown. The graphite coated glasses are the high voltage electrodes and the strip on the copper claded FR4 forms the other electrodes and are grounded(initial study). The dimension of the FR4 used is 27×27 cm^2. The strips are of width 4 cm and are of length 16.3 cm with gap of 1 mm in between them. The strips of the FR4 were designed in `Solidworks` and are printed on photo-paper which is then heat transferred to the copper. The process of heat transfer was not accurate and patches of open copper surfaces were formed and thus, the same graphite paint was used to cover those areas with paint brush. Finally the FR4 is etched with $FeCl_3$ solution to get the desired pattern of the readout. The graphite is removed with thinner to expose the copper according to the design. The strips on one side of the FR4 is perpendicular to the strips to the other side which will give us the position information.

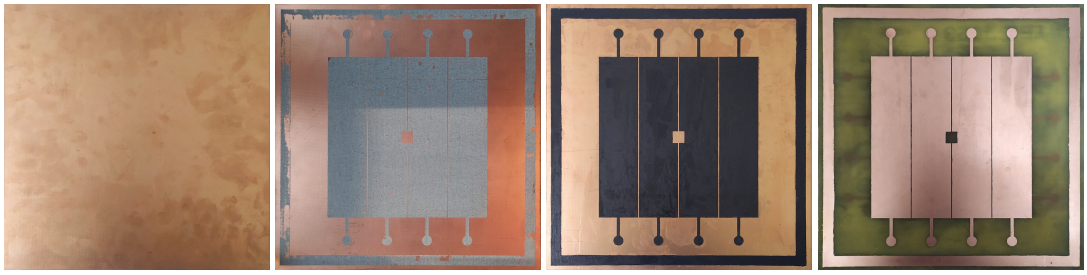

(a) (b) (c) (d)

Figure 5.4: (a) copper claded FR4 (b) strip design after heat transfer (c) graphite coating to cover the patches (d) FR4 after etching.

On one side of the FR4 the secondary electron multiplier layer is coated. The secondary electron multiplier which is a metal oxide. We have used TiO_2(Titanium dioxide) in our RPC. The TiO_2 (nano-particles) is dissolved in ethanol and coated on the strip area with a air brush. It forms good adhesion on the surface but can be removed easily if rubbed, therefore one has to be very careful with the handling of the TiO_2 coated FR_4.

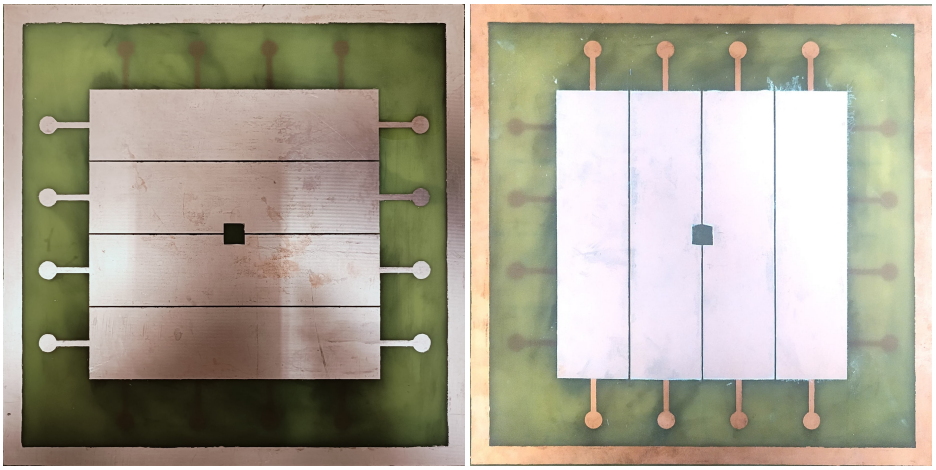

(a) (b)

Figure 5.5: (a) FR4 side without TiO_2 coating and (b)FR4 side with TiO_2 coating.

The glasses and the FR4 are arranged with 2 mm square spacer in between them which is pasted with a double sided tape. The whole setup is kept inside an acrylic box and connection for the high voltage for both the glass plates are made with special insulation cables.

The boundary copper enclosure (1 cm width) of both the FR4s are common grounded. One end of the strips are connected to the ground at the boundary on both sides of the FR4. The signal cable is connected to the other end of the strip and ground of the signal cable is connected to the common ground. These cables are taken out of the acrylic box and the box is sealed such that it is air tight. We have checked for leaks in the acrylic box after sealing it and the possible leaks have been mitigated.

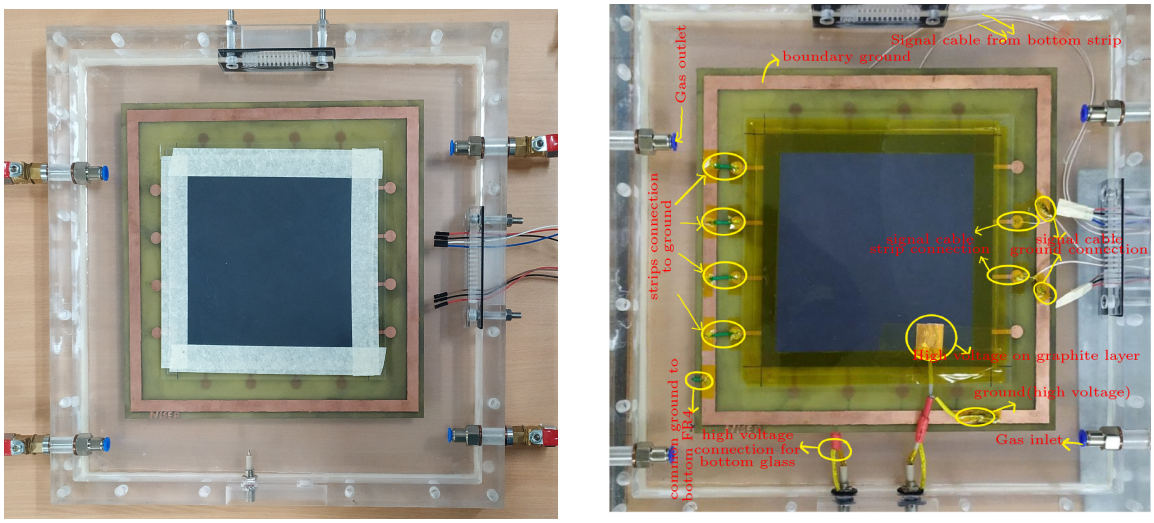

(a) (b)

Figure 5.6: (a)Pre-assembled set-up (b)assembled RPC before closing the chamber.

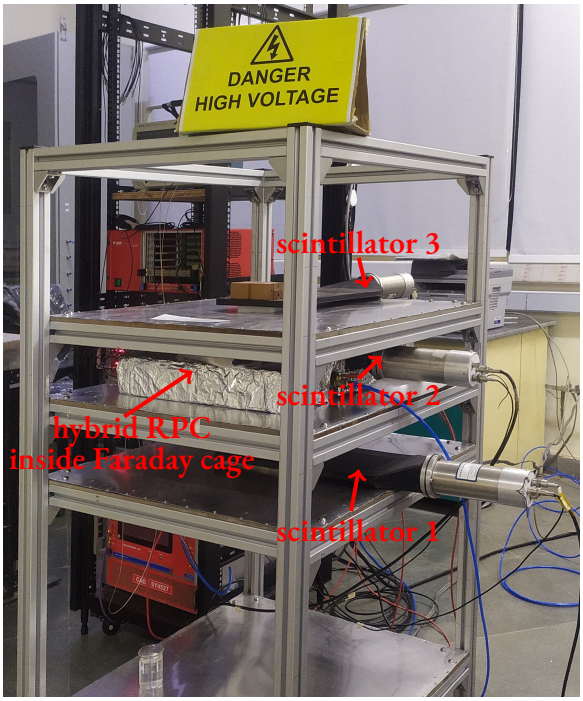

Figure 5.7: The telescope setup for the RPC.

This detector has been arranged with scintillators in a telescope for triggering as shown in Figure 5.7. The scintillator 1 and scintillator 3 are of width 20 cm and the scintillator are of width 4 cm. One strip of the hybrid RPC was activated at a time. The hyrbid RPC has been placed inside

a Faraday cage prepared with aluminium foil to reduce noise. The three scintillators are in AND configuration for the purpose of triggering.

The initial attempt has been with Argon+CO_2 gas composition with ratio of 80:20. The gas break down happens at about $\sim$ 6 kV and we observe discharge.

We observed reflection in the signal with induction on the other side of the FR4 strip as well. The metal electrode readout has been modified further. Instead of using double sided FR4 two single sided FR4s have been arranged with aluminium foil in between them which is connected to the common ground. Along with that the connector to the strip has also been made broad.

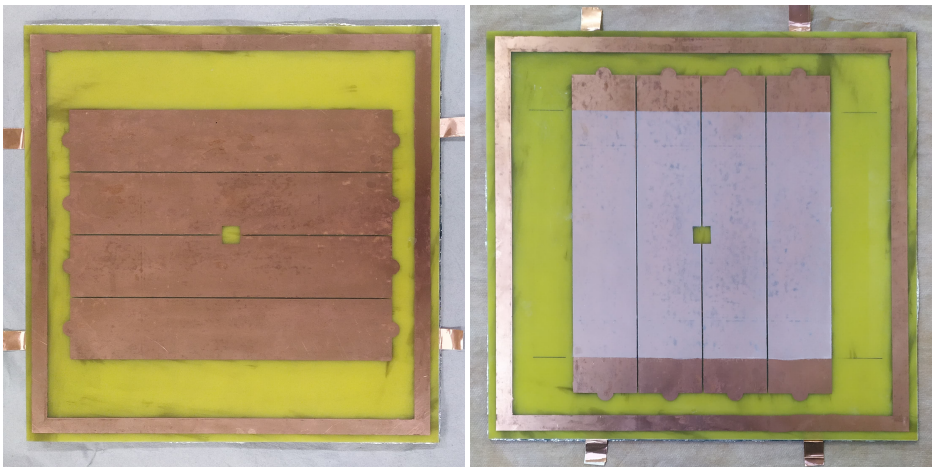

(a) (b)

Figure 5.8: Modified design of the FR4 (a) FR4 side without TiO_2 coating and (b)FR4 side with TiO_2 coating.

With the modified FR4 strip read out, the RPC was tested with standard RPC gas mixture(95.2% R134a, 4.5% Iso-butane, 0.3% SF_6) at 10 cc/m. Furthermore, earlier one end of the strip was used for the read out and the other was grounded, now the one end of the strip is utilised for the read out and the other operated in floating condition.

The current vs Voltage curve for the hybrid RPC for the Ar+CO_2 gas mixture has been shown in the Figure 5.10. The Signal obtained from the hybrid RPC with the Ar+CO_2 gas mixture has been shown in the Figure 5.11a at 4.6 kV and the signal with gas mixture of R134a+C_4H_{10}+SF_6 is shown in Figure 5.11b at 10 kV both operated at 10 cc/m.

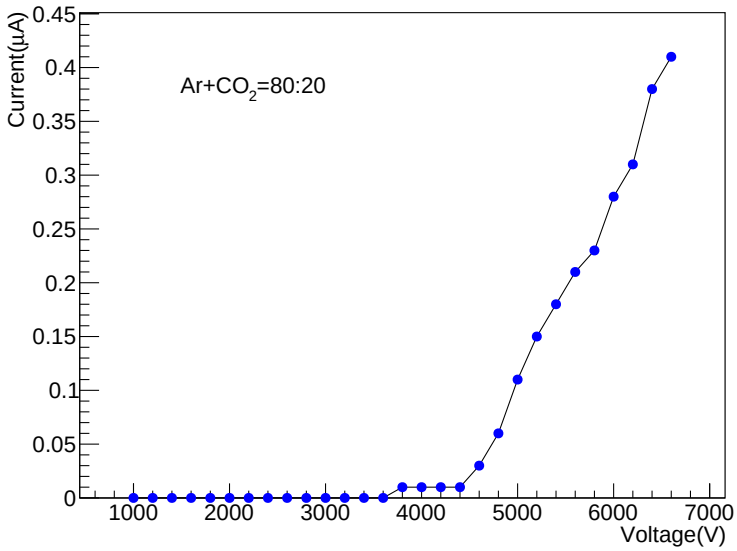

Figure 5.9

Figure 5.10: Current versus voltage curve for the Argon+CO_2 mixture of 80:20 ratio with grounded strips (one end of the strip is connected to the ground).

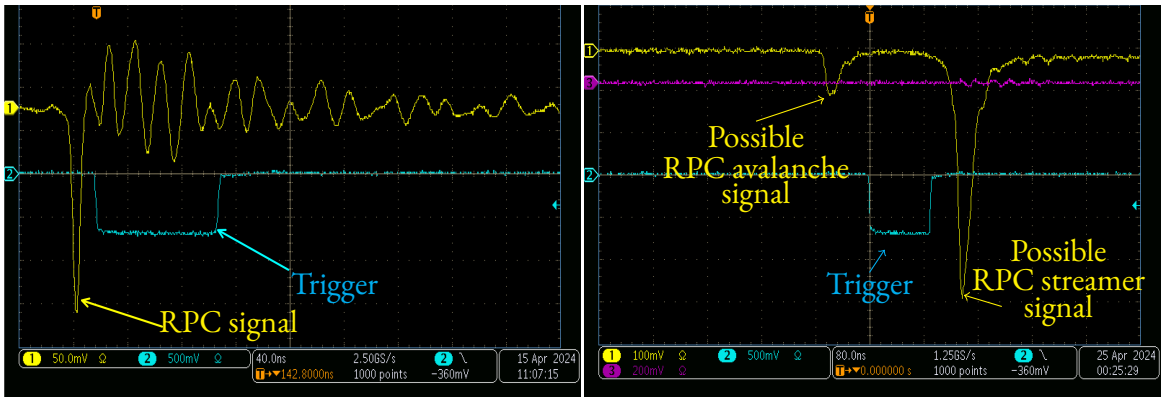

(a) (b)

Figure 5.11: Signal from the hybrid RPC(in yellow), signal from the trigger(in cyan) (a) Argon+CO_2 gas mixture at 4.6KV with strips grounded (b) standard gas mixture (R134a+Isobutane+SF_6) at 10 KV with strips at floating.

Chapter 6

Conclusions and Outlook

We have found the muon detection efficiency in the RPC detector with using Geant4.11.1 and PYTHIA8.309 after simulating pp collisions at 14 TeV and Pb-Pb at 5.52 TeV in PYTHIA and tracking in Geant4. We have implemented the digitization of hits in the RPC to study the effect of granularity. We were also successful in simulating the relativistic charge particle path in the magnetic field and get a single high density $\Delta\eta$-$\Delta\phi$ region in the $\Delta\eta$ and $\Delta\phi$ histogram. It was found that the muon detection efficiency in the pp and Pb-Pb collisions for the magnetic and the non-magnetic case doesn't vary much with the current strip width. The choice of absorber has no effect on the muon detection efficiency and the results are similar. The muon detection efficiency is more than 90% after $p_T > 2$ GeV/c. The maximum background (π and K) efficiency we have found is ∼14%. We have found the J/ψ reconstruction efficiency for the pp collisions and observed that the RPC based detector system have higher J/ψ reconstruction efficiency than the LOI at lower $p_T < 4$ GeV/c of J/ψ both for magnetic and non-magnetic absorber case. At higher p_T the reconstruction efficiency of J/ψ is similar to the LOI for magnetic absorber case and slightly lower than LOI for non-magnetic absorber case. The results do not deviate much from LOI, though the LOI results are with non-magnetic absorber and scintillator. The background can be reduced further with implementation of machine learning to discriminate the muon candidates from the background. The geometry must be implemented in the O^2 analysis framework of ALICE to perform studies with other simulation toolkit such as FLUKA.

We have built a hybrid one glass RPC with secondary electron multiplier TiO_2. The RPC was tested with cosmic muon and signal was found at around 4.6 KeV with Argon and Carbon dioxide gas mixture as well as standard RPC gas mixture at 10 kV. Further investigation and the characterisation of the RPC is required with different gas mixtures.

References

[1] Murray Gell-Mann. A Schematic Model of Baryons and Mesons. *Phys. Lett.*, 8:214–215, 1964.

[2] Cheuk-Yin Wong. *Introduction to High-Energy Heavy-Ion Collisions*. World Scientific, Singapore, 1994.

[3] S.-K. Choi et al. Observation of a Narrow Charmonium like State in Exclusive $B^{\pm} \to K^{\pm}\pi^{+}\pi^{-}J/\psi$ Decays. *Phys. Rev. Lett.*, 91:262001, Dec 2003.

[4] ALICE Collaboration. Letter of intent for ALICE 3: A next-generation heavy-ion experiment at the LHC. CERN-LHCC-2022-009, LHCC-I-038, 11 2022. `https://arxiv.org/abs/2211.02491`.

[5] A. Andronic, P. Braun-Munzinger, M. K. Köhler, et al. The multiple-charm hierarchy in the statistical hadronization model. *Journal of High Energy Physics*, 2021(35):035, 2021.

[6] M. Tosun, B. Bilki, and K.K. Sahbaz. Development of hybrid resistive plate chambers. *Nuclear Instruments and Methods in Physics Research Section A: Accelerators, Spectrometers, Detectors and Associated Equipment*, 1054:168448, 2023.

[7] K. Nakamura and et al. Review of particle physics. *Journal of Physics G: Nuclear and Particle Physics*, 37:075021, 2010.

[8] R. Santonico and R. Cardarelli. Development of resistive plate counters. *Nuclear Instruments and Methods in Physics Research*, 187(2):377–380, 1981.

[9] Solidworks. online. `https://www.3ds.com/products/solidworks`.

[10] Christian Bierlich et al. A comprehensive guide to the physics and usage of pythia 8.3, 2022. arXiv:2203.11601.

[11] J. Allison et al. Geant4 developments and applications. *IEEE Transactions on Nuclear Science*, 53(1):270–278, 2006.

[12] J. Allison et al. Recent developments in Geant4. *Nuclear Instruments and Methods in Physics Research Section A: Accelerators, Spectrometers, Detectors and Associated Equipment*, 835:186–225, 2016.

[13] S. Agostinelli et al. Geant4—a simulation toolkit. *Nuclear Instruments and Methods in Physics Research Section A: Accelerators, Spectrometers, Detectors and Associated Equipment*, 506(3):250–303, 2003.

[14] René Brun and Fons Rademakers. Root - an object-oriented data analysis framework. *Nucl. Inst. & Meth. in Phys. Res. A*, 389:81–86, 1997. `https://root.cern/download/lj.ps.gz` Paper published in the Linux Journal, Issue 51, July 1998.

[15] Arpan Maity. Msc thesis code, 2024. `https://github.com/maityarpan`.

[16] Particle Data Group. Monte carlo simulations in particle physics, 2007. `https://pdg.lbl.gov/2007/reviews/montecarlorpp.pdf`.

[17] Marc Paterno. Calculating efficiencies and their uncertainties, 2004. `https://lss.fnal.gov/archive/test-tm/2000/fermilab-tm-2286-cd.pdf`,accessed 21 April 2024.

[18] Varchaswi K S Kashyap. *Studies on Resistive Plate Chambers (RPC) for INO and scintillators for reactor antineutrino detection*. PhD thesis, Homi Bhabha National Institute, Anushaktinagar, Mumbai - 400094, India, 2016.

[19] Torbjörn Sjöstrand, Leif Lönnblad, and Stephen Mrenna. Pythia 6.2 physics and manual, 2001. arXiv:hep-ph/0108264.

Appendix A

Resistive Plate Chambers

A.1 Construction

An RPC (Resistive Plate Chamber) comprises of two flat electrodes crafted from resistive materials such as bakelite or glass, with a bulk resistivity ranging from 10^{10} to 10^{12} Ω cm, depending on the material. These electrodes are coated with a conductive paint, such as graphite, to facilitate the application of high voltage. The glass or bakelite electrode are positioned at a close distance of approximately 1 to 3 mm, separated by cylindrical button spacers made of PVC or polycarbonate. This gap is filled with a suitable gas mixture. The assembly is sealed from all sides using edge spacers made of PVC or polycarbonate, and nozzles are incorporated to facilitate gas flow. The signals are extracted with readouts made of copper strips which are coupled capacitatively to the electrode using an insulating material (e.g. Mylar/PET sheet). An illustration of the RPC [18] is given in Figure A.1. The generally used gas mixture is Freon-r134a (95.2%), iso-butane (4.5%) and SF_6 (0.3%).

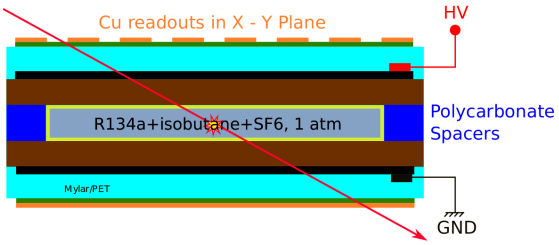

Figure A.1: Illustration of RPC

A.2 Working

When a charged particle enters the gas mixture within the RPC, it undergoes energy loss, leading to the ionization and excitation of molecules. Ionization can occur either through the interaction of the charged particle with the electron of an atom with the Coulomb field (distant interaction) or through collisions between the charged particle and the atom's electron (close interaction). If the atom gets excited, it may release energy by emitting a photon or by emitting Auger electrons. The RPC signal is generated via electron multiplication. As the incoming particle traverses the gas mixture, clusters of primary electrons are produced through ionization. Under the influence of a strong electric field, these electrons migrate towards the anode, generating additional electron and ion pairs. The formation of an avalanche in a gas detector can be elucidated by applying Townsend's theory given by,

$$n = n_0 \exp{(\alpha - \beta)x} \tag{A.1}$$

where n_0 is the number of electrons in the cluster, n is the number of electrons reaching the anode, α is the first Townsend coefficient which is the number of ionizations per unit length, β is the attachment coefficient which is the number of electrons captured by the gas molecules per unit length and x is the distance from the primary cluster to the anode. α and β are the characteristic of the used gas. The gain is defined as the ratio,

$$G = \frac{n}{n_0} \tag{A.2}$$

A.2.1 Modes of Operation

Avalanche

When the gas gain (G) in the RPC is small (less than $\sim 10^8$), the Townsend avalanche formed lacks the ability to generate secondary avalanches. Consequently, the signal strength of the RPC remains relatively low, necessitating the use of low-noise pre-amplification electronics to effectively utilize the signal without compromising the timing characteristics of the RPC. The region of the RPC that becomes insensitive to incident radiation is contingent upon the quantity of charge produced in the gas. Given the limited amount of charge generated, the RPC demonstrates a commendable capability to handle rates, approximately around 1 kHz/cm^2.

Streamer

When the voltage is elevated, yielding a gas gain (G) exceeding 10^8, photons generated through excitation and recombination start to play a role in the multiplication process, giving rise to secondary avalanches. Consequently, a substantial current, known as a streamer, is produced, leading to the formation of a conductive channel between the electrodes. The resulting signal is robust, and the RPC doesn't necessitate any pre-amplification electronics. However, due to the increased amount of charge generated, the dead time is extended, thereby reducing the rate handling capability to approximately 100 Hz/cm^{-2} .

Mode	Gas composition(%)			
	Argon	Freon-r 134a	Iso-butane	SF_6
Avalance	-	95.2	4.5	0.3
Streamer	30	60	8	2

Table A.1: Typical composition of gases in RPC.

A.2.2 Role of the gases

Argon

Argon is an inert gas used in RPC in streamer mode as tabulated in Table A.1. Argon is employed in gas detectors because it is readily accessible, cost-effective, demands relatively high ionization energy, and possesses effective stopping power against incident radiation.

Freon-r134a

Freon regulates the development of the avalanche and has a slightly electronegative nature. In the context of RPCs operating in the avalanche mode, Freon acts as the medium for the interaction with incident radiation.

Iso-butane

During the ionization process primarily involving freon, the ions and electrons generated in the signal may undergo recombination, leading to the production of UV photons. These photons, in turn, generate undesired pulses in other parts of the detector. Iso-butane is capable of absorbing and converting the energy of these photons into vibrational states. Due to the combustible nature

of iso-butane, its concentration in the gas mixture is always maintained below the flammability limit.

SF_6

It possesses a electronegative character, playing a crucial role in halting the development of the avalanche. Functioning as a quenching gas, it effectively diminishes the formation of streamers.

Appendix B

Simulation of RPC with Geant4 and PYTHIA

B.1 PYTHIA

It is a Monte-Carlo event generator widely used in high energy physics [10]. Initially, PYTHIA was a framework to study the pp collision. Later on, the Angantyr framework was introduced to study heavy ion collisions as well. The Angantyr framework models the Nucleus with the geometry of Nucleons as a 2-Dimensional wood Saxon distribution. The collisions are simulated with a Lorentz contracted condition of the nucleus at a very small range of time and space ($t = z = 0$). A set of separate hadron–hadron (HH) interactions are defined in PYTHIA/Angantyr for A-A collision, where the hadron can be either a nucleon or a pomeron-like object. The hadronization in PYTHIA is modelled with string fragmentation mechanism. The chronological sequence of the physics aspects that are followed by PYTHIA is as follows:

1. The initial phase consists of two beams of particles approaching each other, each possessing parton distributions that outline their partonic substructure in terms of flavor composition and the distribution of energy.

2. A parton from each beam initiates a sequence of branchings, like $q \rightarrow qg$, starting an initial-state shower.

3. One incoming parton from each shower enters the hard process, generating a set of outgoing partons, typically two, with the nature of this process determining the event's main characteristics.

4. The hard process may produce short-lived resonances (e.g., $Z^0/W^{\pm}$ gauge bosons) whose decay to normal partons needs consideration in conjunction with the hard process.

5. Outgoing partons may undergo branching, similar to the incoming ones, contributing to the formation of final-state showers.

6. Apart from the main hard process, additional semi-hard interactions may occur among other partons from the two incoming hadrons.

7. When a shower initiator is removed from a beam particle, a beam remnant remains, potentially having an internal structure and a net color charge connected to the final state.

8. The QCD confinement mechanism ensures that outgoing quarks and gluons are not observable, fragmenting into color-neutral hadrons.

9. Typically, the fragmentation process is viewed as occurring in separate color singlet subsystems, although interconnection effects like color rearrangement or Bose–Einstein statistics may complicate the scenario.

10. Many of the generated hadrons are unstable and undergo further decay processes.

All the above mentioned points are simulated in a sequential order in PYTHIA and which is common for much of all event generators. The further decay additions in terms of decay and re-scattering are also included in PYTHIA in recent development [19].

B.2 Geant4

Geant-4 is a toolkit where we can define detectors geometries of various shapes and sizes and simulate particle interactions [11, 12, 13]. It also allows to import geometries from commercially available 3D modelling software like Solidworks, AutoCAD etc. We initially tried to import them in the project but faced issues related to detector referencing. We proceeded with the modelling of detectors in the standard procedure within Geant4. Geant4 also allows tracking of particles in electric and magnetic fields. The sensitive part of the geometry where one would expect signals to be detected in real life are called as sensitive detectors in Geant4. From the sensitive detectors, one can obtain physical parameters of the particles such as position, energy, time, momentum, particle charge, parent, daugther etc. The framework includes many physics lists or interactions namely, electron-magnetic physics, weak interaction physics, hadronic physics etc. In our study we have considered the physics list `FTFP_BERT`. For this physics list the hadronic section compilation includes elastic, inelastic, capture, and fission processes. Each of these processes is con-

structed using a collection of cross-section sets and interaction models, offering a comprehensive implementation of the underlying physics details.

B.3 Using PYTHIA with Geant4

Geant-4 is integrated with PYTHIA. Events of pp collisions at 14 TeV are generated using Pythia and the particles with decay time greater than $\sim 10^{-10}$ s are propagated in Geant-4. Geant-4 uses the physics interactions with the detector geometry, materials and provides different physical parameters of the particles and their daughters.

Appendix C

Simulation results

selection criteria (matching window)

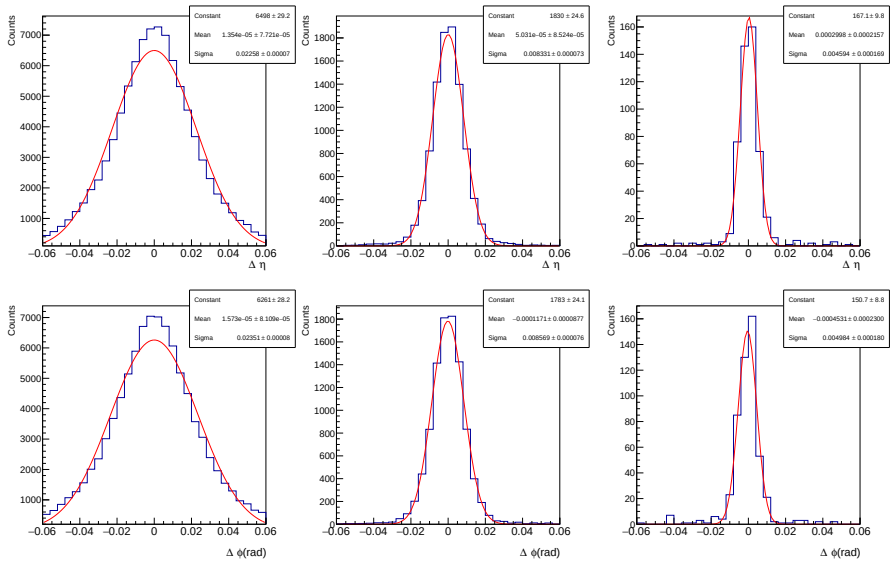

(a) $p_T < 2$GeV/c (b) $2 < p_T < 5$GeV/c (c) $p_T > 5$GeV/c

Figure C.1: $\Delta\eta$ and $\Delta\phi$ matching window for pp collisions with non-magnetic absrober for RPC layer 1. The top row is for $\Delta\eta$ and the bottom row is for $\Delta\phi$ for the 3 different p_T range in the columns.

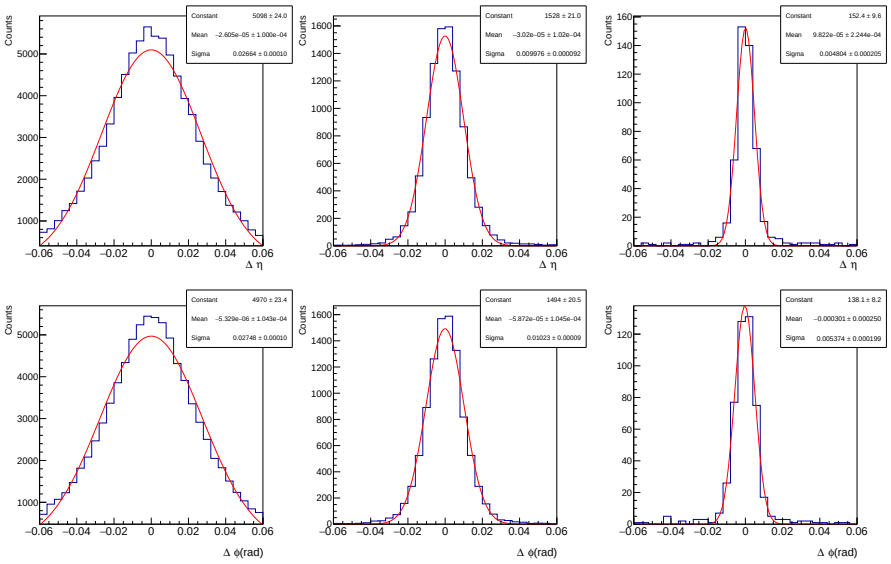

(a) $p_T < 2$GeV/c (b) $2 < p_T < 5$GeV/c (c) $p_T > 5$GeV/c

Figure C.2: $\Delta\eta$ and $\Delta\phi$ matching window for pp collisions with non-magnetic absrober for RPC layer 2. The top row is for $\Delta\eta$ and the bottom row is for $\Delta\phi$ for the 3 different p_T range in the columns.

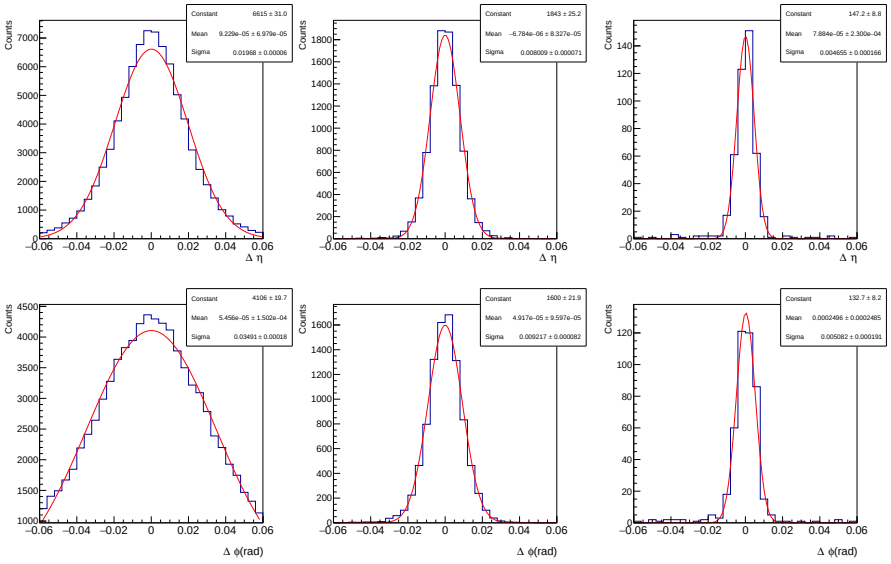

(a) $p_T < 2$GeV/c (b) $2 < p_T < 5$GeV/c (c) $p_T > 5$GeV/c

Figure C.3: $\Delta\eta$ and $\Delta\phi$ matching window for pp collisions with magnetic absrober for RPC layer 1. The top row is for $\Delta\eta$ and the bottom row is for $\Delta\phi$ for the 3 different p_T range in the columns.

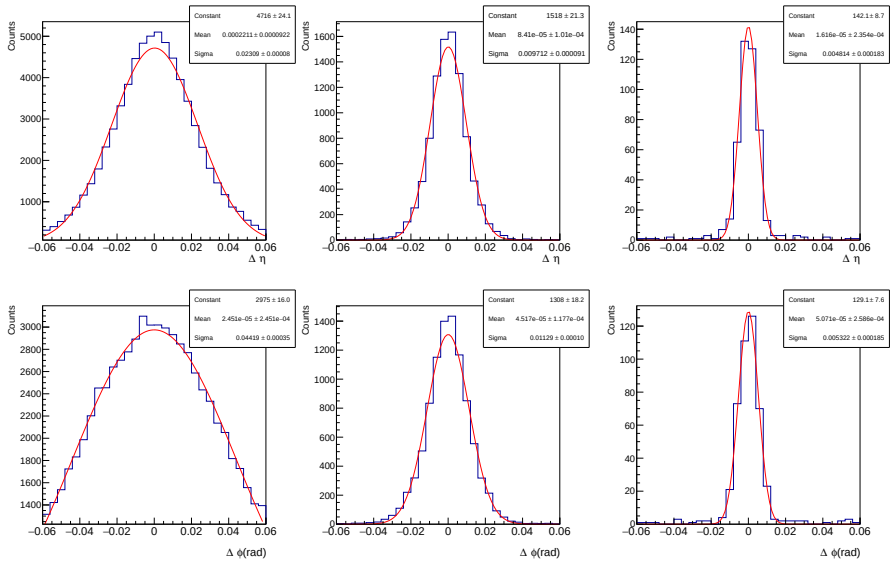

(a) $p_T < 2$GeV/c (b) $2 < p_T < 5$GeV/c (c) $p_T > 5$GeV/c

Figure C.4: $\Delta\eta$ and $\Delta\phi$ matching window for pp collisions with magnetic absrober for RPC layer 2. The top row is for $\Delta\eta$ and the bottom row is for $\Delta\phi$ for the 3 different p_T range in the columns.

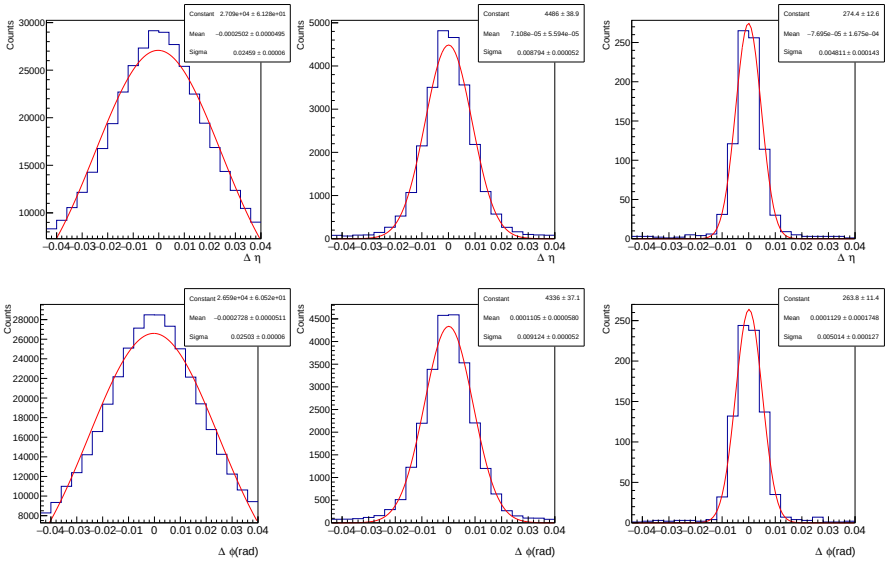

(a) $p_T < 2$GeV/c (b) $2 < p_T < 5$GeV/c (c) $p_T > 5$GeV/c

Figure C.5: $\Delta\eta$ and $\Delta\phi$ matching window for Pb-Pb collisions with non-magnetic absrober for RPC layer 1. The top row is for $\Delta\eta$ and the bottom row is for $\Delta\phi$ for the 3 different p_T range in the columns.

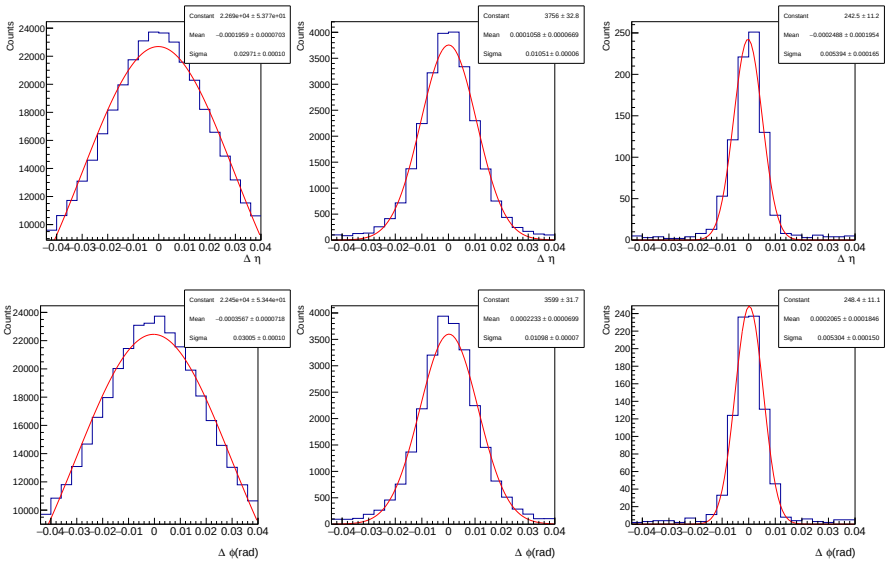

(a) $p_T < 2$GeV/c (b) $2 < p_T < 5$GeV/c (c) $p_T > 5$GeV/c

Figure C.6: $\Delta\eta$ and $\Delta\phi$ matching window for Pb-Pb collisions with non-magnetic absrober for RPC layer 2. The top row is for $\Delta\eta$ and the bottom row is for $\Delta\phi$ for the 3 different p_T range in the columns.

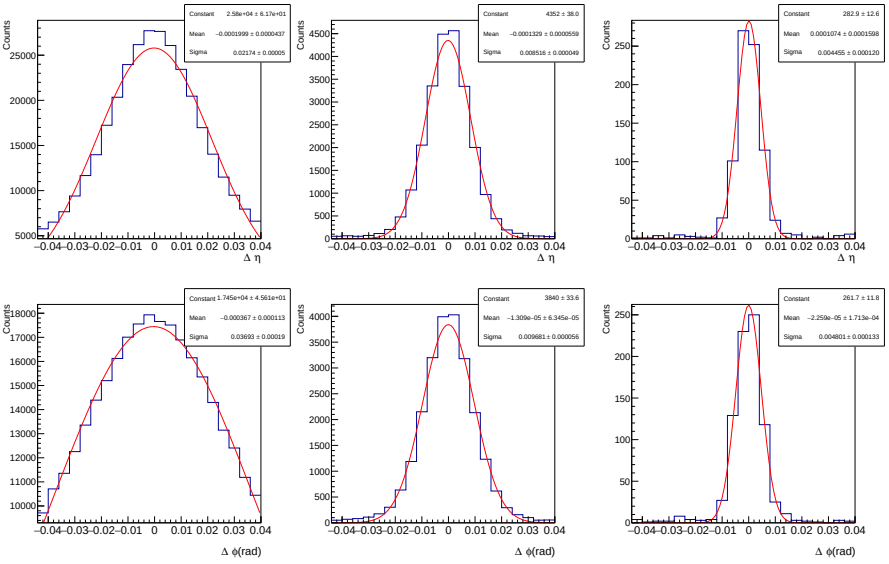

(a) $p_T < 2$GeV/c (b) $2 < p_T < 5$GeV/c (c) $p_T > 5$GeV/c

Figure C.7: $\Delta\eta$ and $\Delta\phi$ matching window for Pb-Pb collisions with magnetic absrober for RPC layer 1. The top row is for $\Delta\eta$ and the bottom row is for $\Delta\phi$ for the 3 different p_T range in the columns.

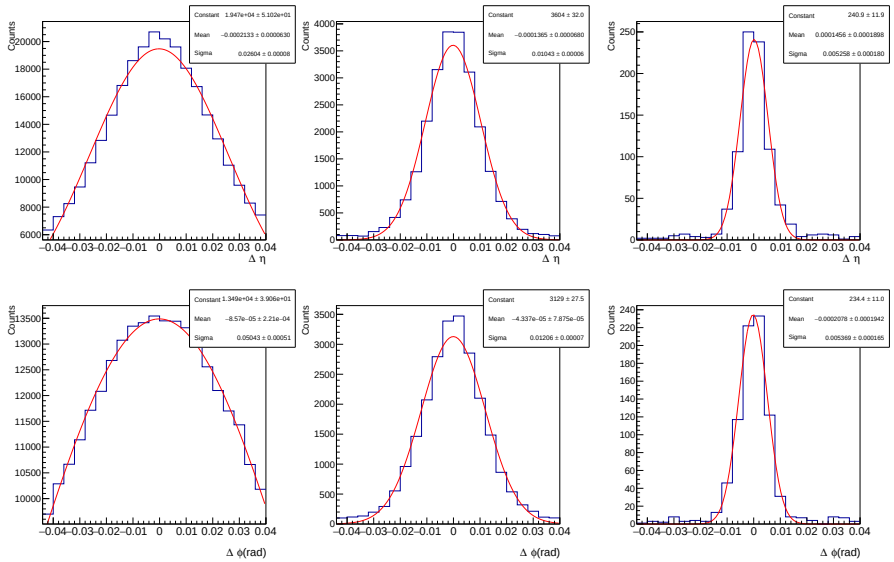

(a) $p_T < 2$GeV/c (b) $2 < p_T < 5$GeV/c (c) $p_T > 5$GeV/c

Figure C.8: $\Delta\eta$ and $\Delta\phi$ matching window for Pb-Pb collisions with magnetic absrober for RPC layer 2. The top row is for $\Delta\eta$ and the bottom row is for $\Delta\phi$ for the 3 different p_T range in the columns.